

1 **1D, 2D and 3D Monte Carlo ambient noise tomography**  
2 **using a dense passive seismic array installed on the**  
3 **North Sea seabed**

4 **Xin Zhang<sup>1</sup>, Fredrik Hansteen<sup>2</sup>, Andrew Curtis<sup>1,3</sup> and Sjoerd de Ridder<sup>4</sup>**

5 <sup>1</sup>School of Geosciences, University of Edinburgh, Edinburgh, United Kingdom

6 <sup>2</sup>Equinor ASA, Bergen, Norway

7 <sup>3</sup>Department of Earth Sciences, ETH Zürich, Switzerland

8 <sup>4</sup>School of Earth and Environment, University of Leeds, United Kingdom

9 **Key Points:**

- 10 • We observe two Scholte wave modes in ambient noise cross-correlations and sep-  
11 arate them using a dispersion compensation method.
- 12 • We applied Eikonal tomography to obtain phase velocity maps for both the fun-  
13 damental mode and the first higher mode.
- 14 • We compared 1D, 2D and 3D Monte Carlo to invert dispersion data for shear ve-  
15 locity and show that the 3D method gives most accurate results.

---

Corresponding author: Xin Zhang, [x.zhang2@ed.ac.uk](mailto:x.zhang2@ed.ac.uk)

## 16 Abstract

17 In a variety of geoscientific applications we require 3D maps of properties of the Earth's  
 18 interior, and the corresponding map of uncertainties to assess their reliability. On the  
 19 seabed it is common to use Scholte wave dispersion data to infer these maps using inversion-  
 20 based imaging theory. Previously we introduced a 3D fully nonlinear Monte Carlo to-  
 21 mography method that inverts for shear velocities directly from frequency-dependent travel  
 22 time measurements, and which improves accuracy of the results and better estimates un-  
 23 certainties. Here for the first time we apply that method to real data and compare it to  
 24 two of those previous methods. We cross correlated 6.5 hours of ambient noise data recorded  
 25 on a dense seismic array over Grane, North Sea, and observed two Scholte wave modes.  
 26 For each mode, phase velocity maps are estimated using Eikonal tomography, which are  
 27 in turn used to study the shear-wave velocity structure of the subsurface. We applied  
 28 three nonlinear inversion methods to the Grane data: standard 1D depth inversions, a  
 29 2D joint inversion along a vertical cross-section, and a fully 3D inversion. We compare  
 30 the shear-velocity and uncertainty structures estimated along the same 2D cross-section.  
 31 Thus we show that the standard 1D inversion method causes errors in the results due  
 32 to independence of those 1D inversions, whereas the 2D and 3D inversions improve re-  
 33 sults by accounting for lateral spatial correlations. The 3D inversion bypasses the ini-  
 34 tial seabed Eikonal tomography step, and therefore avoids the errors it introduces into  
 35 subsequent 1D and 2D inversions.

## 36 1 Introduction

37 Geoscientists often need to image or monitor the subsurface in order to understand  
 38 the properties and processes of the Earth's interior. Seismic tomography is a technique  
 39 which has been used widely to produce three-dimensional models of the properties of the  
 40 Earth. In order to interpret the imaging results appropriately, and in particular to avoid  
 41 over-interpretation, it is often desirable to estimate uncertainties in such models.

42 Seismic surface waves propagate along interfaces in the Earth across which seis-  
 43 mic properties change abruptly (Rayleigh and Love surface waves propagate along the  
 44 Earth's surface, i.e. the interface between solid and air, whereas Scholte waves propagate  
 45 along the seabed at the interface between liquid and solid), and oscillate over depth ranges  
 46 that depend on frequency (Aki & Richards, 1980). This in turn makes surface waves dis-  
 47 persive – different frequencies travel at different speeds, and these speeds are sensitive

48 to different parts of the Earth. By measuring the wave speeds this dispersion property  
49 can therefore be used to study the subsurface of the Earth by tomographic imaging on  
50 global (Trampert & Woodhouse, 1995; N. Shapiro & Ritzwoller, 2002; Meier et al., 2007a,  
51 2007b; Ferreira et al., 2010; Ekström, 2011) and regional scales (Zielhuis & Nolet, 1994;  
52 Curtis et al., 1998; Simons et al., 2002; Y. Yang et al., 2007; Lin et al., 2008; Zigone et  
53 al., 2015).

54 In the above studies, surface waves were generated by earthquakes, which inevitably  
55 limits the resolvability of models in regions of sparse coverage due to the inhomogeneous  
56 distribution of seismic sources and stations. The introduction of ambient noise interfer-  
57 ometry has greatly increased the size and coverage of our surface wave datasets by turn-  
58 ing receivers into virtual (imagined) sources. It has been shown theoretically that Green's  
59 functions between different receiver pairs can be retrieved by cross correlations of am-  
60 bient noise data recorded at the receivers (Campillo & Paul, 2003; Wapenaar, 2004; van  
61 Manen et al., 2005, 2006; Wapenaar & Fokkema, 2006; Curtis et al., 2006). Surface waves  
62 contained in the Green functions can be extracted and used to study subsurface struc-  
63 ture (N. M. Shapiro & Campillo, 2004). This method has been used widely to study the  
64 regional scale structure of crust and uppermost mantle (N. M. Shapiro et al., 2005; Yao  
65 et al., 2006; Lin et al., 2007, 2009; Y. Yang et al., 2007; Yao & Van Der Hilst, 2009; Bensen  
66 et al., 2009; Behr et al., 2010; Nicolson et al., 2012, 2014) and the near surface upper-  
67 most crustal structure (de Ridder & Dellinger, 2011; de Ridder & Biondi, 2013; Mordret,  
68 Landès, et al., 2013; Mordret, Shapiro, et al., 2013; Mordret, Landès, et al., 2014; de Rid-  
69 der et al., 2014, 2015; Allmark et al., 2018).

70 In most of the above studies only the fundamental mode surface wave is used due  
71 to the fact that higher modes are often so low in amplitude as to be invisible in the data.  
72 However, in surface waves generated by earthquakes it has been shown that higher modes  
73 can be observed (Gabriels et al., 1987; Park, Miller, & Xia, 1999; Park, Miller, Xia, Hunter,  
74 & Harris, 1999) and can be used to further constrain the subsurface structure (Gabriels  
75 et al., 1987; Jan van Heijst & Woodhouse, 1999; Xia et al., 2000, 2003). Mordret, Shapiro,  
76 and Singh (2014) also observed higher modes in the cross correlations of ambient noise  
77 data recorded by ocean bottom cable (OBC) sensors over the Valhall oil field, but since  
78 this energy was much weaker than the fundamental mode, these higher modes were ig-  
79 nored. However, in other cases the energy of higher modes can be comparable to the fun-  
80 damental mode and may cause errors in inferred fundamental mode phase or group ve-

81 locities due to the fact that the modes are mixed together (Xia et al., 2003). Therefore,  
82 it is important to correctly identify and separate the different modes.

83 If multiple source-receiver distances are available, higher modes can often be sep-  
84 arated from fundamental modes by frequency-wavenumber (F-K) analysis (Gabriels et  
85 al., 1987). However, this process assumes that speeds of each frequency are the same for  
86 all source-receiver pairs. In order to perform phase or group velocity tomography, we of-  
87 ten need accurate phase/group velocity measurements from each mode for each source-  
88 receiver pair independently. This means that individual modes need to be separated at  
89 each receiver. This can be done by band-pass filtering if the modes occupy different fre-  
90 quency bands (Crampin & B ath, 1965), but unfortunately this is not always the case.  
91 Other methods based on adaptive wavelet transformations (Kritski et al., 2006; Kuttig  
92 et al., 2006) or mode-branch stripping (van Heijst & Woodhouse, 1997) have been pro-  
93 posed to quantify the energy of individual modes and to separate them, but those meth-  
94 ods risk destroying the phase of individual modes, and thus introducing errors in the phase  
95 velocity picks. In this study we therefore used a method based on dispersion compen-  
96 sation (Wilcox, 2003; Xu et al., 2012) or equivalently on time reversal (Fink, 1992; Al-  
97 leyne et al., 1993; Ing & Fink, 1998). In this method, an individual mode in a disper-  
98 sive wave is compressed to a short-duration pulse in the time domain by adjusting the  
99 phase to undo the dispersion so that each mode can be separated easily from the oth-  
100 ers e.g., by using a time-windowing function. The method has been used successfully to  
101 separate Lamb modes in ultrasonic waves (Xu et al., 2012), but has not previously been  
102 applied to seismic surface waves.

103 Seismic surface wave inversion problems are often solved using a 2-step scheme of  
104 first inverting for two-dimensional (2D) geographical maps of surface wave phase or group  
105 velocity and then inverting for the 3D spatial velocity structure using 1D inversions for  
106 structure over depth beneath each geographical location (Nakanishi & Anderson, 1983;  
107 Trampert & Woodhouse, 1995; Ritzwoller et al., 2002; Snoke & Sambridge, 2002; Bodin  
108 & Sambridge, 2009; Bodin et al., 2012; Galetti et al., 2017). The 2D tomographic prob-  
109 lem in the first step is usually solved by a linearized procedure by minimizing the data  
110 misfit while applying some regularization (Trampert & Woodhouse, 1995; Ritzwoller et  
111 al., 2002). However, the regularization is often chosen by ad hoc means (often trial and  
112 error), and it can suppress valuable information (Zhdanov, 2002). It has also been shown  
113 to be difficult to quantify meaningful uncertainties from linearized ambient noise tomog-

114 raphy (N. Shapiro & Ritzwoller, 2002; Bensen et al., 2009; Yao & Van Der Hilst, 2009;  
115 Weaver et al., 2011; Nicolson et al., 2012, 2014). As a result the 1D depth inversions in  
116 the second step can be affected by biased 2D velocity and uncertainty estimation (Young  
117 et al., 2013).

118 To resolve these issues nonlinear inversion methods based on the Markov chain Monte  
119 Carlo (MCMC) sampling algorithm have been introduced to seismic tomography (Mosegaard  
120 & Tarantola, 1995). MCMC is a class of methods which generate samples from a target  
121 probability density (Metropolis & Ulam, 1949; Hastings, 1970; Mosegaard & Tarantola,  
122 1995; Sivia, 1996; Malinverno et al., 2000; Malinverno, 2002; Malinverno & Briggs, 2004).  
123 In seismic tomography, a generalised MCMC method called the *reversible jump* algorithm  
124 (Green, 1995; Green & Hastie, 2009) is often used; this allows a trans-dimensional in-  
125 version to be carried out, which means that the dimensionality of the parameter space  
126 (the number of model parameters) can vary in the inversion (Bodin & Sambridge, 2009;  
127 Hawkins & Sambridge, 2015; Piana Agostinetti et al., 2015; Burdick & Lekić, 2017; Galetti  
128 et al., 2017; Galetti & Curtis, 2018). In these methods, a class of model parametriza-  
129 tion is dynamically adapted to both the prior information and the data. The method  
130 has been used to estimate phase and group velocity maps of the crustal structure (Bodin  
131 & Sambridge, 2009; Zulfakriza et al., 2014; Galetti et al., 2015; Zheng et al., 2017) and  
132 to carry out the second depth-inversion step to obtain 3D shear wave velocity structures  
133 of the crust and uppermost mantle (Bodin et al., 2012; Shen et al., 2012, 2013; Young  
134 et al., 2013; Galetti et al., 2017).

135 However, Zhang et al. (2018) showed that due to the independence of the many 1D  
136 inversions in the second step and possible phase or group velocity errors introduced in  
137 the first step, the 2-step method causes biases in estimated 3D shear-wave velocity mod-  
138 els no matter whether linearized or MCMC methods are used. They proposed an alter-  
139 native 3D Monte Carlo method that directly inverts frequency-dependent phase or group  
140 traveltimes measurements in one step, and showed via synthetic tests that the method  
141 improves accuracy of the velocity model estimation and produces more intuitively rea-  
142 sonable uncertainties than the traditional 2-step method. A similar idea has also been  
143 used with a linearized inversion method (Fang et al., 2015). In this study we apply the  
144 3D Monte Carlo method to study the near surface structure of the Grane field and com-  
145 pare the results to those generated using previous methods.

146 The Grane oil field is situated in the North Sea, about 185 km west of the city of  
147 Haugesund, Norway with a water depth of 127m (Figure 1) and contains heavy crude  
148 oil found in turbidite sandstone from the Tertiary period (Pragt et al., 2012). It was first  
149 discovered by Norsk Hydro in 1991 and is currently operated by Equinor ASA. It started  
150 production in 2003, which is estimated to last for 25 years. The field is composed of one  
151 main reservoir and a few other segments at a depth of 1,700 m. A permanent monitor-  
152 ing system has been deployed in the field, which contains 3458 four-component sensors  
153 (Z-vertical, N-north, E-east component and H-hydrophone). This records seismic data  
154 from the field continuously (Thompson et al., 2015) and thus provides the possibility to  
155 use ambient noise tomography to monitor the reservoir.

156 In the following we first present the ambient noise data and compute their cross  
157 correlations to obtain Scholte waves in section 2. In section 3 we briefly describe the dis-  
158 persion compensation method and use it to separate the different Scholte wave modes.  
159 In section 4 we determine phase velocity maps for both the fundamental mode and the  
160 first overtone using Eikonal tomography. In section 5 we first review the standard 2-step  
161 method and the new 3D method, then apply them to estimate the shear-wave velocity  
162 structure over the Grane field. For the 2-step inversion, the phase velocity maps in sec-  
163 tion 3 are used as data. To further understand the limitation of independent 1D inver-  
164 sions, we also performed a 2D inversion using a 2D parameterization of a 2D cross-section  
165 using the same data as in the 1D depth inversions. We then compare all results across  
166 the 2D section. We conclude that the 3D Monte Carlo inversion method produces more  
167 realistic results, and achieves this with comparable computation cost compared to the  
168 standard 2-step Monte Carlo method.

## 169 **2 Ambient noise interferometry at Grane field**

### 170 **2.1 Noise data recorded by the permanent monitoring system at Grane** 171 **field**

172 Figure 1 shows the locations of all 3458 sensors over the Grane field, each of which  
173 records samples at 500 Hz. The depth of the sea floor is around 127 m, becoming slightly  
174 shallower in the northeast (120 m). The sensors are organized along linear cables and  
175 consequently have inline and crossline spacings of approximately 50 m and 300 m respec-  
176 tively. This permanent and continuously recording array provides the potential to use

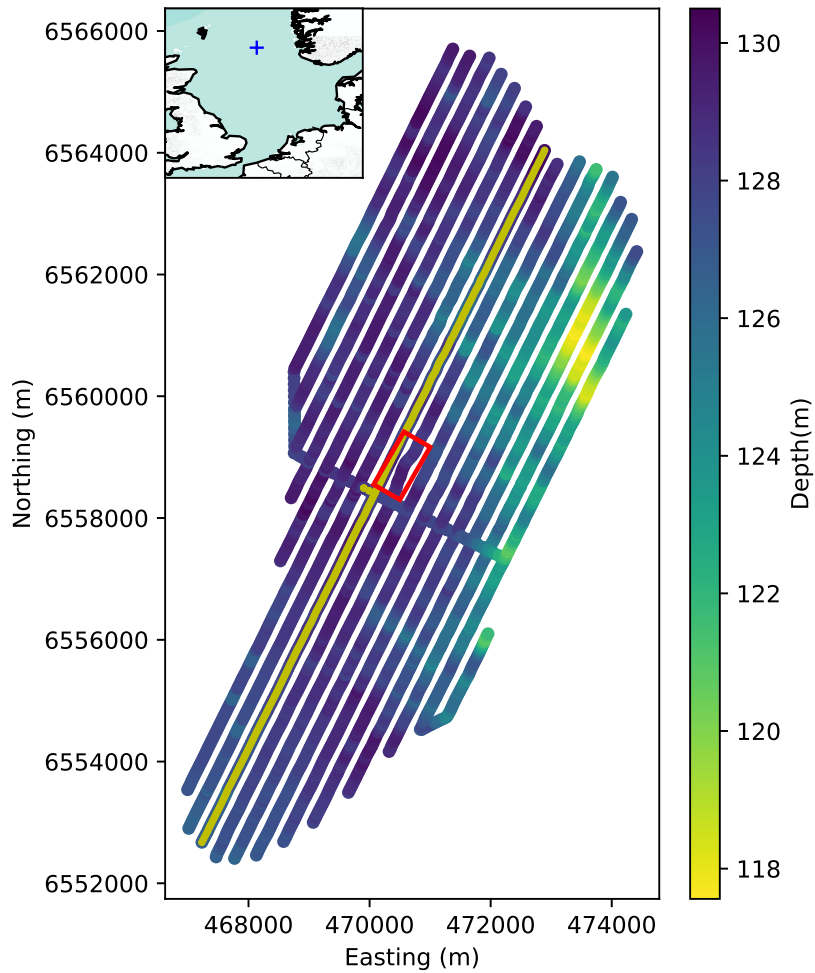


**Figure 1.** The distribution of receivers at the Grane field coloured according to their depths below sea level. The red box shows the location of the platform and the yellow line shows a receiver line used in the text. The blue plus in the inset map indicates the location of Grane field.

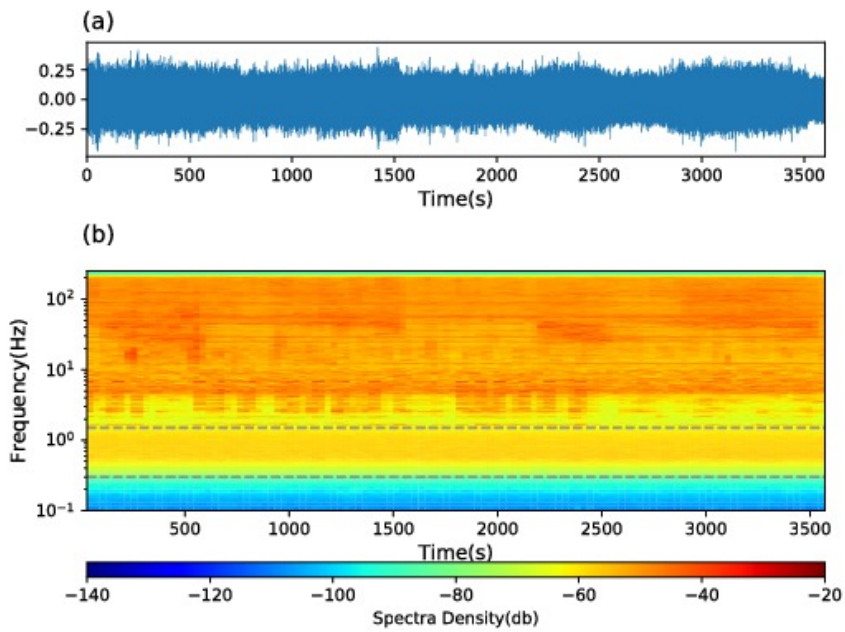


**Figure 2.** (a) An example of one-hour of vertical component data recorded by one of the geophones at Grane field; and (b) the corresponding spectrogram. The gray dashed lines bound the frequency range used for cross correlations.

177 passive seismic interferometry for daily monitoring of the field. In this study, we there-  
 178 fore analysed only 6 hours and 36 minutes of continuous data extracted from recordings  
 179 in November 2014.

180 We analysed spectrograms of one-hour intervals of vertical component data extracted  
 181 from those 6.5 hours of data. Figure 2a shows an example of one such dataset from one  
 182 receiver. Figure 2b shows the spectrogram of energy across frequency as a function of  
 183 time computed using 1 minute windows with 50% overlap between windows. The spec-  
 184 trogram is cut off below 0.3 Hz due to the roll-off in receiver sensitivity. The typical fre-  
 185 quency response of the receivers is from 3 Hz to 15 KHz. However, it has been shown  
 186 that lower frequency data can still be used for ambient noise studies (de Ridder & Dellinger,  
 187 2011; Mordret, Landès, et al., 2013, 2014). For example, between 0.3 Hz and 1.5 Hz the  
 188 data are dominated by the tail of the secondary microseismic peak (Webb, 1998) and  
 189 can be used to estimate Scholte waves from noise cross correlations. Above 1.5 Hz, field-  
 190 operation noise sources and active seismic sources dominate the data. While it is also  
 191 possible to obtain useful information about the subsurface using high frequency data (Mordret,  
 192 Landès, et al., 2013), in this study we focus on the frequency band between 0.3 Hz and  
 193 1.5 Hz to obtain Scholte waves and use them to study the near surface structure.

194 The Scholte waves obtained from noise cross correlations can be biased in the case  
 195 of an inhomogeneous distribution of noise sources (Wapenaar, 2004; Curtis & Halliday,  
 196 2010). Therefore we used the beamforming technique (Cole, 1995; Rost & Thomas, 2002)  
 197 to characterize the noise distribution of Grane field. The recordings were first band-filtered  
 198 into a narrow bands (e.g. 0.4-0.6 Hz) to avoid possible blurring of the beamforming re-  
 199 sults caused by velocity dispersion. The data were then transformed to  $\tau - p$  domain  
 200 by slant stacking (Yilmaz, 2001). Here we carried out beamforming analysis using half-  
 201 hour segments for all receivers together. Figure 3 shows results for two frequency bands:  
 202 0.4-0.6 Hz and 0.6-0.8 Hz. Both results show two circles with different phase velocities,  
 203 which are associated with different Scholte waves modes. The fundamental mode has a  
 204 phase velocity of  $\sim 580$  m/s at the lower band (0.4-0.6 Hz) and a phase velocity of  $\sim 520$   
 205 m/s at the higher band (0.6-0.8 Hz) while the corresponding phase velocity of the first  
 206 overtone is  $\sim 910$  m/s and  $\sim 830$  m/s respectively in each band. Note that the energy of  
 207 either side of the 0.6-0.8 Hz result is spatial aliasing due to the cross-line sparsity of re-  
 208 ceivers (Yilmaz, 2001). Although there is residual inhomogeneity, for example, at the lower  
 209 frequency band the energy in the west is slightly higher than in the east, in both cases

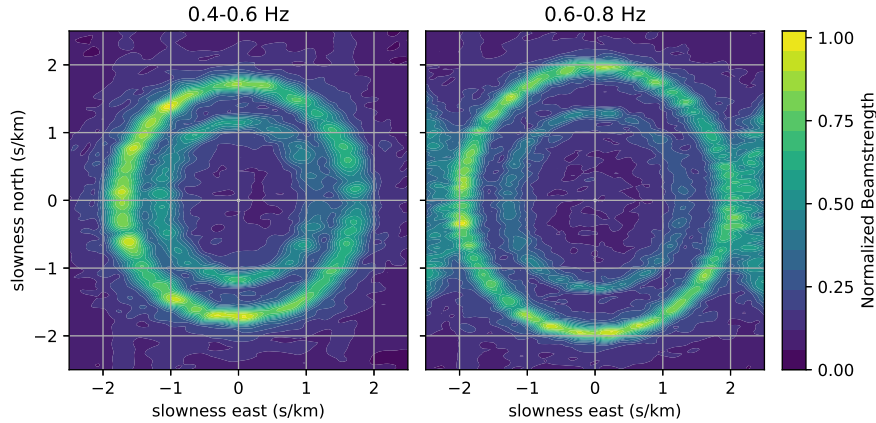


**Figure 3.** The beamforming results of two narrow frequency bands: 0.4-0.6 Hz (left) and 0.6-0.8 Hz (right) calculated using half-hour data segments.

210 the noise sources are nearly omnidirectional for both modes, which implies that we have  
 211 sufficiently equidistributed noise sources for noise-based interferometry and tomography.

## 212 **2.2 Cross-correlations of ambient noise**

213 Seismic ambient noise interferometry refers to the construction of Green’s functions  
 214 from virtual sources by noise cross correlations (Campillo & Paul, 2003; Wapenaar, 2004;  
 215 Curtis et al., 2006). The data are first bandpass-filtered to 0.35-1.50 Hz using a frequency  
 216 domain taper, and down-sampled to 5 Hz sampling rate. Spectral-whitening is then ap-  
 217 plied to create data with a uniform amplitude spectrum. This process is carried out us-  
 218 ing half-hour recording segments with a 50% overlap. Finally the data from every sta-  
 219 tion pair are cross correlated segment by segment and results are stacked over the 6.5  
 220 hour interval. We did not remove instrument responses because they are identical for  
 221 all receivers. In this study, we only obtained cross correlations using vertical (Z) com-  
 222 ponents and hydrophone components (H) to construct Rayleigh-type waves, but it would  
 223 be possible to construct Love waves using north (N) and east (E) components in future  
 224 (Mordret, Landès, et al., 2013).

225 Figure 4a and 4d show virtual shot gathers along a receiver line indicated in Fig-  
 226 ure 1 (yellow line) constructed using pairs of vertical components and pairs of hydrophone  
 227 components respectively. At long distances the wave packet spreads out in time due to

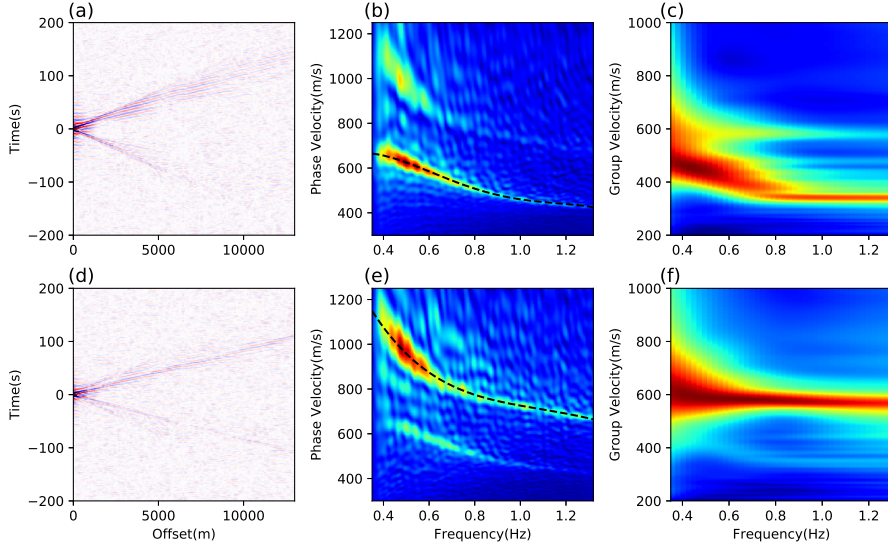


**Figure 4.** Examples of virtual shot gathers constructed using (a) vertical components and (d) hydrophone components. The receivers used are shown in Figure 1. (b) and (e) show the associated phase velocity dispersion analysis using  $f - c$  analysis where  $c$  is phase velocity, and (c) and (f) show the associated group velocity dispersion analysis. The black dashed lines indicate the picked phase velocity for the fundamental mode and first overtone.

228 dispersion. The negative time part has smaller energy than the positive time part, es-  
 229 pecially at long distances. This may be caused by some residual inhomogeneity in the  
 230 distribution of noise sources (Figure 3), or some deviation of the noise sources from the  
 231 ideal sources assumed in theory (mutually uncorrelated point sources).

To analyse the Scholte wave dispersion, we carried out frequency-phase velocity ( $f-c$ ) analysis for the virtual shot gathers in Figure 4a and Figure 4d. The  $f-c$  spectrum  $U(c, f)$  of gather  $u(x, t)$  is computed using:

$$U(c, f) = \iint_{-\infty}^{+\infty} u(x, t) e^{j2\pi f(t - \frac{x}{c})} dx dt \quad (1)$$

232 where  $x$  is distance along the virtual shot gather,  $t$  is time,  $f$  is frequency,  $c$  is phase ve-  
 233 locity and  $j = \sqrt{-1}$ . For this research we used the symmetric part of the correlation  
 234 results  $u(x, t)$  (the mean of the positive and negative time results) after testing that this  
 235 at least did not appear to be detrimental to results and appeared to increase stability  
 236 of results. The results (Figure 4b, e) clearly show the two modes that we observed us-  
 237 ing beamforming analysis (Figure 3). Phase velocity varies from 420 m/s to 660 m/s for

238 the fundamental mode and from 660 m/s to 1150 m/s for the first overtone. The fun-  
 239 damental mode dominates the signal in the vertical component cross correlations while  
 240 in the hydrophone components the first overtone dominates, which has been observed  
 241 before (Savage et al., 2013; Tomar et al., 2018) and has been shown to be related to a  
 242 few hundred meters of low velocity sediments below the sea floor (Tomar et al., 2018).

243 We also analyse group velocity dispersion. Group velocities can be obtained by us-  
 244 ing the traditional frequency-time analysis (FTAN) method (Dziewonski et al., 1969; A. L. Lev-  
 245 shin et al., 1972; A. Levshin et al., 1992; Herrin & Goforth, 1977; Russell et al., 1988;  
 246 Ritzwoller & Levshin, 1998; A. Levshin & Ritzwoller, 2001; Yanovskaya et al., 2012). For  
 247 each seismic trace, a frequency-time domain envelope image can be obtained by apply-  
 248 ing a Hilbert transform for a set of narrow frequency bands (e.g. by narrow-band Gaus-  
 249 sian filters). To estimate the group velocities for possible different modes, we stacked all  
 250 those envelope images across the receiver line in Figure 1 to improve signal to noise ra-  
 251 tio (Figure 4c, f). Similarly to the phase velocity dispersion analysis, the two modes can  
 252 be observed in the stacked envelope image. The group velocity of the fundamental mode  
 253 decreases from 480 m/s to 350 m/s from 0.35 Hz to 0.8 Hz and then shows very little  
 254 variations after 0.8 Hz. By contrast, the group velocities of the first overtone varies only  
 255 slightly from 610 m/s to 590 m/s over the frequency range from 0.35 Hz to 1.3 Hz.

### 256 **3 Mode separation**

257 Although it is often the case that only one mode dominates the signal in a wave  
 258 (the energy of the first overtone is usually lower than the fundamental mode in vertical  
 259 component recordings - Figure 4b, c), energy from other modes will still cause bias in  
 260 the phase or group velocity of each seismic trace (e.g., Xia et al., 2003). For example,  
 261 at low frequencies ( $< 0.5$  Hz) the group velocities of the two modes are very close and  
 262 probably cannot be identified individually easily, which may cause biases in phase or group  
 263 velocity picking (see below). This could produce errors in subsequent tomography re-  
 264 sults. Therefore, in order to obtain accurate phase or group velocity picks for each trace  
 265 and for each mode, we first need to separate the modes.

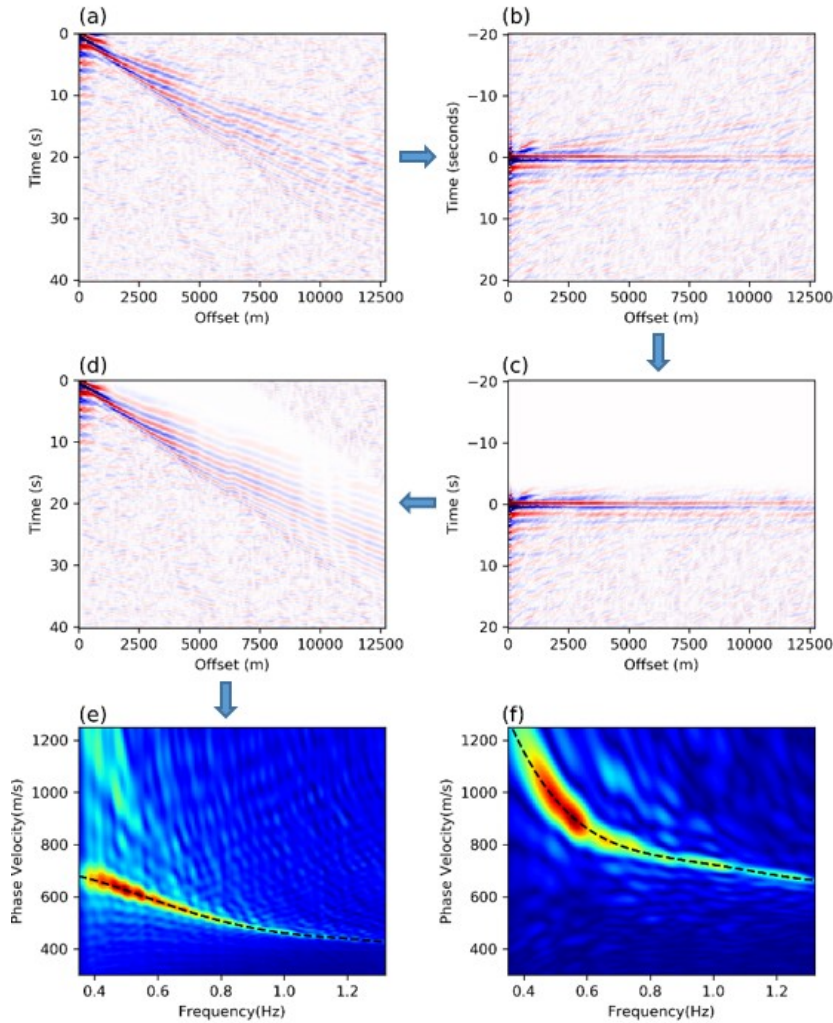


**Figure 5.** An example of the mode separation procedure. (a) The virtual shot gather before mode separation (obtained from Figure 4a by adding positive and negative times). (b) Flattened virtual shot gather obtained by dispersion compensation. (c) Filtered flattened virtual shot gather. (d) Virtual shot gather after mode separation. (e) Phase velocity dispersion analysis after mode separation. (f) Phase velocity dispersion analysis after using a similar method to instead isolate the first overtone. Arrows show the order of processing steps. Black dashed lines show the associated phase velocity dispersion curves.

266

### 3.1 Method

We use a dispersion compensation method to separate different modes (Xu et al., 2012). For seismic surface waves we assume that two modes  $S$  and  $A$  are excited by a broadband source excitation  $F(w)$ , and that the phase velocity of the modes are constant across the area. In the frequency domain the recorded surface wave at distance  $x_0$  can then be expressed as

$$G_{SA}(w) = [Amp_S H_S(w) + Amp_A H_A(w)]F(w) \quad (2)$$

267

268

269

270

271

where  $H_S(w) = \exp(-jk_S(w)x_0)$  and  $H_A(w) = \exp(-jk_A(w)x_0)$ ,  $k_S(w)$  and  $k_A(w)$  are dispersion relations of mode  $S$  and mode  $A$  respectively, and  $Amp_S$  and  $Amp_A$  are their amplitudes. If  $k_S(w)$  and  $k_A(w)$  are known, the process of dispersion can be reversed by back-propagation or dispersion compensation. For example, multiplying equation (2) by  $H_S^{-1}(w) = \exp(jk_S(w)x_0)$  gives

$$\begin{aligned} G_{SA}^*(w) &= H_S^{-1}(w)G_{SA}(w) \\ &= Amp_S F(w) + Amp_A H_S^{-1}(w)H_A(w)F(w) \end{aligned} \quad (3)$$

272

273

274

275

276

277

278

where  $G_{SA}^*(w)$  is the surface wave after dispersion compensation. The first term  $Amp_S F(w)$  has no dispersion (propagation) term so will be focused to a short-duration pulse  $f(t)$  in time domain at zero time, which can be extracted using a window function. The second term is the residual term from mode  $A$  which is still dispersive. After separating mode  $S$  from the other waves, it can be propagated back to distance  $x_0$  by multiplying the extracted signal by  $H_S(w)$ . The result then can be used to estimate more accurate phase or group velocities for mode  $S$ , and a similar operation can be used to extract mode  $A$ .

279

280

281

282

283

284

285

286

In practice, the dispersion relations  $k_S(w)$  or  $k_A(w)$  are usually not constant across the area of study. However, they often vary smoothly across space at least locally. So equation (3) can still be used for approximate dispersion compensation. Alternatively, one can integrate along estimated source to receiver ray path to estimate the correct dispersion to each receiver if an approximate estimate of the phase velocity map is known. This dispersion estimate can then be used for  $k_S(w)$  or  $k_A(w)$  as appropriate. In this study, we simply applied equation (3) using estimates of dispersion relations (picked from an initial frequency-wavenumber analysis such as that shown in Figure 4).

287

### 3.2 Application to Grane field

288

289

290

291

292

293

294

295

296

297

298

299

300

301

302

303

304

305

306

307

308

309

310

311

312

313

314

We used the method above to separate different modes across Grane field. The data were first back-propagated to time zero in the frequency domain using equation (3) using the dispersion relation of the fundamental mode picked using  $f-c$  analysis (black dashed line in Figure 4b), and then transformed back to the time domain. Figure 5b shows the results after dispersion compensation for the symmetric part of the virtual shot gather in Figure 4a. The symmetric gather is shown in Figure 5a. After dispersion compensation, the fundamental mode focuses to an impulsive signal at zero time so that energy in the shot gather becomes flat. Those waves that exist at negative time and are not flat are higher modes since higher modes generally travel faster than the fundamental mode. They can be muted using a time-domain window function (Figure 5c). Figure 5d shows the shot gather after windowing out the higher modes and transforming back to the original propagation time. Figure 5e shows the dispersion image obtained from  $f-c$  analysis using the virtual shot gather after mode separation (Figure 5d). At most frequencies (0.5 - 1.3 Hz) the energy of the first overtone disappears, indicating that the higher modes have been removed successfully. However, at low frequencies (0.35-0.5 Hz) some energy from the first overtone remains. This can be explained by the fact that at these frequencies (0.35 - 0.5 Hz) the group velocities of the two modes are very close (Figure 4c) which leads to the modes overlapping even after back-propagation to time zero.

Similarly to the separation of the fundamental mode, we apply the method to obtain waves containing higher modes only. Since the first overtone dominates the signal in cross correlations of hydrophone components (Figure 4e, f), we used those cross correlations to retrieve the first overtone. The phase velocity dispersion curve picked from the result of  $f-c$  analysis (Figure 4e) is used to carry out the phase correction. The fundamental mode is then windowed out using a window function and consequently waves containing only the first overtone are obtained (Figure 5f). Finally, after mode separation we obtain Scholte waves that contain only the fundamental mode or the first overtone, which can be used to pick accurate phase or group velocities for each mode.

## 4 Phase velocity tomography

### 4.1 Method

To perform phase or group velocity tomography, we first need to pick phase or group velocities for each cross correlation between each station-pair. There are so many pairs that this process must be automated. Group velocity can be picked using the FTAN method (see description in section 2.2). For phase velocity picking we used an image transformation technique (Yao et al., 2006). First a time-period image ( $t - T$ ) is constructed by applying a set of narrow-band filters to the data. This can be transformed to a velocity-period image ( $c - T$ ) by transforming time to phase velocity, for the moment assuming a straight-ray path between each station pair (Figure 6). Finally the phase velocity dispersion curve can easily be identified and automatically picked on the  $c-T$  image. The  $2\pi$  ambiguity of phase velocity measurements can be resolved using our initial estimate of the average phase velocity dispersion curve obtained using  $f-c$  analysis (black line in Figure 4b; white line in Figure 6).

To improve the quality of dispersion data, we applied a series of data selection criteria. A minimum signal to noise ratio (SNR) of 5 is used for the fundamental mode and 2.5 is used for the first overtone. The SNR is calculated using the spectrum of the signals of interest and the spectrum of an interval of noise extracted from the end of the virtual source records. Due to the far-field approximation that is implicit in the ambient noise interferometry method, those station-pairs whose distances are smaller than twice the wavelength at any frequency are discarded (Yao et al., 2006; Lin et al., 2009). Considering the possible biases introduced by mode separation in the frequency range of 0.35 - 0.5 Hz (2 - 2.85 s period) – see Figure 5e – in phase velocity tomography we only used phase velocities at frequencies larger than 0.5 Hz ( $< 2$  s period).

We picked phase velocities and group velocities for each station-pair, which can then be used to perform phase or group velocity tomography. Group velocity tomography can be conducted using straight-ray tomography since the data accuracy usually does not merit a more sophisticated approach and since an accurate phase velocity map is not available in order to trace rays to allow group velocity to be calculated along rays (de Ridder & Dellinger, 2011; Mordret, Landès, et al., 2013; Allmark et al., 2018). However, since that the phase velocity measurements are more accurate than group velocities (Yao et al., 2006) and since Eikonal tomography is more efficient and more accurate than straight-

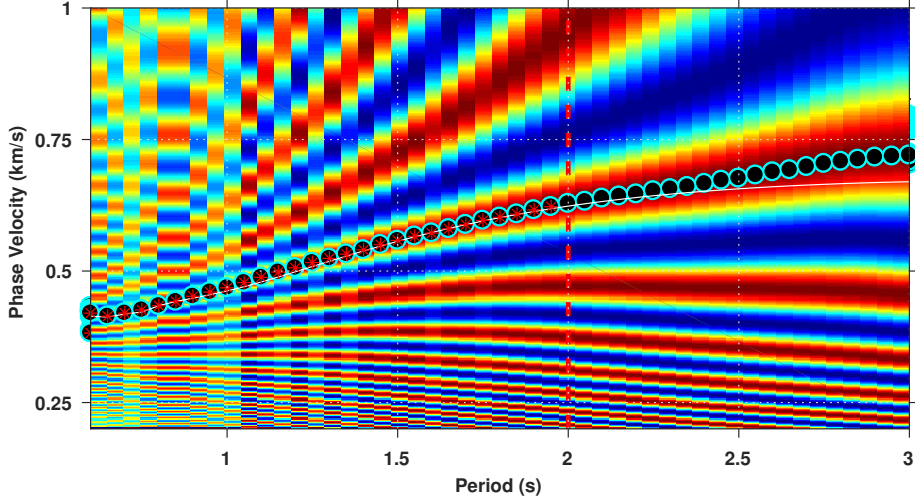


**Figure 6.** An example of the  $c - T$  image used to pick phase velocities. The dashed black line shows the maximum period allowed by the far-field approximation (the offset must be larger than twice the wavelength). The black dots denote the picked phase velocity for the whole period range and the red stars show phase velocities that are actually used. The white line shows the phase velocity dispersion curve obtained using  $f - c$  analysis.

347 ray tomography (Lin et al., 2009), we performed phase velocity tomography using the  
 348 Eikonal method as we now describe.

In a smoothly heterogeneous medium, the propagation of a single surface wave mode can be expressed using the Eikonal equation (Aki & Richards, 1980; Biondi, 1992; Wielandt, 1993; Shearer, 1999):

$$\frac{1}{c_i(w, \mathbf{r})^2} = |\nabla \tau_i(w, \mathbf{r})|^2 - \frac{\Delta A_i(w, \mathbf{r})}{A_i(w, \mathbf{r})w^2} \quad (4)$$

where  $c$  is the phase velocity,  $\tau$  is the travel time,  $A$  is the spectral amplitude,  $w$  is the angular frequency,  $\mathbf{r}$  is the location, and subscript  $i$  denotes the  $i^{th}$  source. If the second term on the right-hand side can be ignored (see discussion in Lin et al. 2009), this equation becomes:

$$\frac{1}{c_i(w, \mathbf{r})} = |\nabla \tau_i(w, \mathbf{r})| \quad (5)$$

349 In this case the local phase slowness at location  $\mathbf{r}$  is simply related to the magnitude of  
 350 the gradient of the travel time field. Therefore, the local phase velocity can be determined  
 351 using equation (5) by calculating the gradient of the travel time field from each virtual  
 352 source (Lin et al., 2009).

353 In order to determine the gradient of the travel time field, we first interpolate the  
 354 travel time field to a regular grid (Lin et al., 2009). Here we used the biharmonic spline  
 355 interpolation to interpolate the field to a  $50m \times 50m$  grid (de Ridder & Dellinger, 2011).  
 356 To better control the quality of the interpolated field, for each location we only use in-  
 357 terpolated travel times that are surrounded by four measurements. Due to small SNR  
 358 at large offsets we discarded measurements whose offsets are greater than 6km.

Finally, the average phase slowness  $s_0(x)$  at location  $x$  and its standard deviation  $\sigma_{s_0}(x)$  can be computed using all virtual sources by

$$s_0(x) = \frac{1}{n} \sum_{i=1}^n s_i(x) \quad (6)$$

$$\sigma_{s_0}^2(x) = \frac{1}{n(n-1)} \sum_{i=1}^n (s_i(x) - s_0(x))^2 \quad (7)$$

where  $n$  is the number of sources and  $i$  denotes the  $i^{th}$  source. Thereafter the phase velocity  $c_0$  and its uncertainty  $\sigma_{c_0}$  can be determined by:

$$c_0(x) = \frac{1}{s_0(x)} \quad (8)$$

$$\sigma_{c_0}(x) = \frac{1}{s_0(x)^2} \sigma_{s_0}(x) \quad (9)$$

## 359 4.2 Results

360 We applied Eikonal tomography for both the fundamental mode and the first over-  
 361 tone in the period range 0.7 s to 2 s. The final mean phase velocity map and its stan-  
 362 dard deviation are averaged over the 3458 sources for each period. Figure 7 shows the  
 363 results of fundamental mode tomography at periods 0.7 s, 1.0 s, 1.3 s and 1.6 s. At short  
 364 periods ( $< 1.6$  s), there is a clear low velocity anomaly in the middle of the field (loca-  
 365 tion delineated by the blue solid line box in the 1s period map). At the west edge be-  
 366 tween  $Y=8$  km and  $Y=10$  km, a clear low velocity anomaly exists at 0.7 s which fades  
 367 out from 1.0 s to 1.3 s. At 0.7 s a low velocity channel connects this low velocity anomaly  
 368 to the middle low velocity anomaly. However, it disappears at longer periods ( $> 0.7$  s),  
 369 which indicates that this is probably a very near surface structure. Instead at periods  
 370 of 1 s and 1.3 s, there is a high velocity channel from middle west to north east (loca-  
 371 tion delineated by white solid line box in the 1s period map) which is interrupted by the  
 372 low velocity channel at 0.7 s. Next to this high velocity channel there is a parallel low  
 373 velocity channel (location delineated by the black dashed line box) existing at short pe-  
 374 riods ( $< 1.6$  s). In the south, a low velocity anomaly also emerges (location delineated

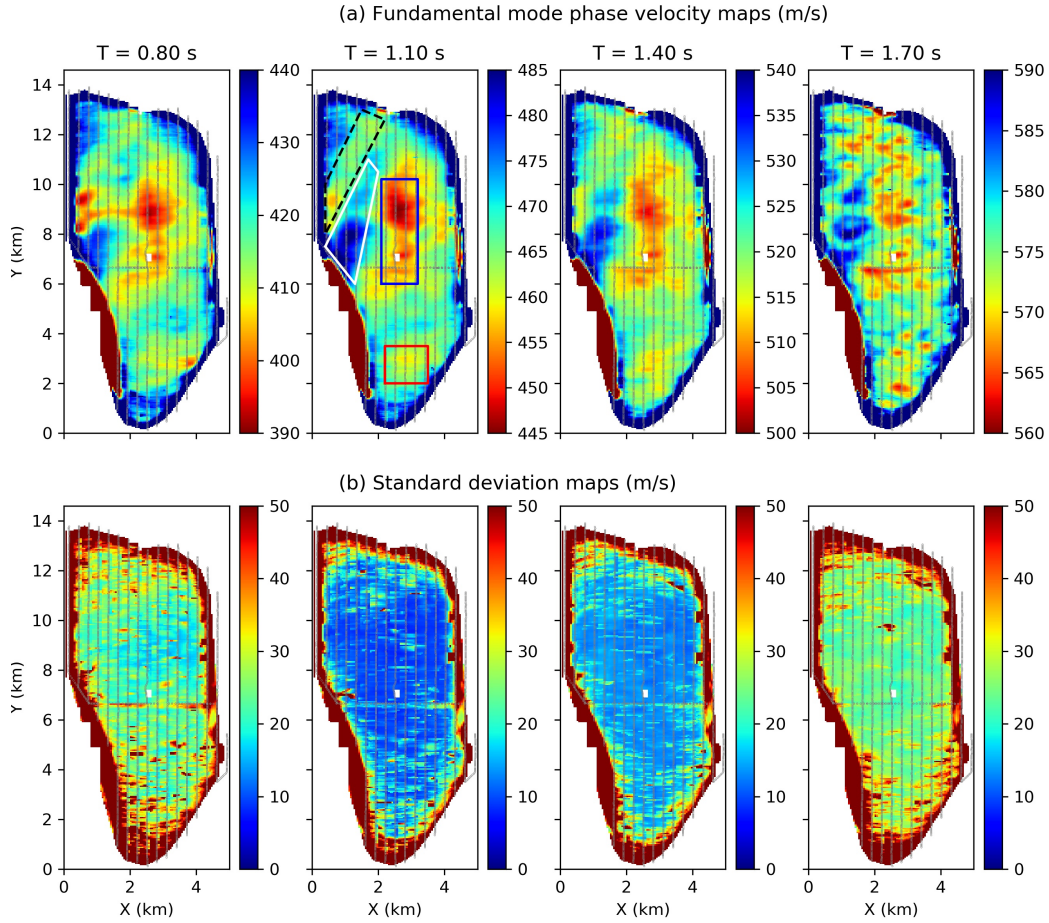


**Figure 7.** (a) Phase velocity maps of the fundamental mode and (b) their associated standard deviation maps at periods 0.7s, 1.0s, 1.3s and 1.6s. The boxes show locations of features discussed in the text. Gray lines show the distribution of receivers.

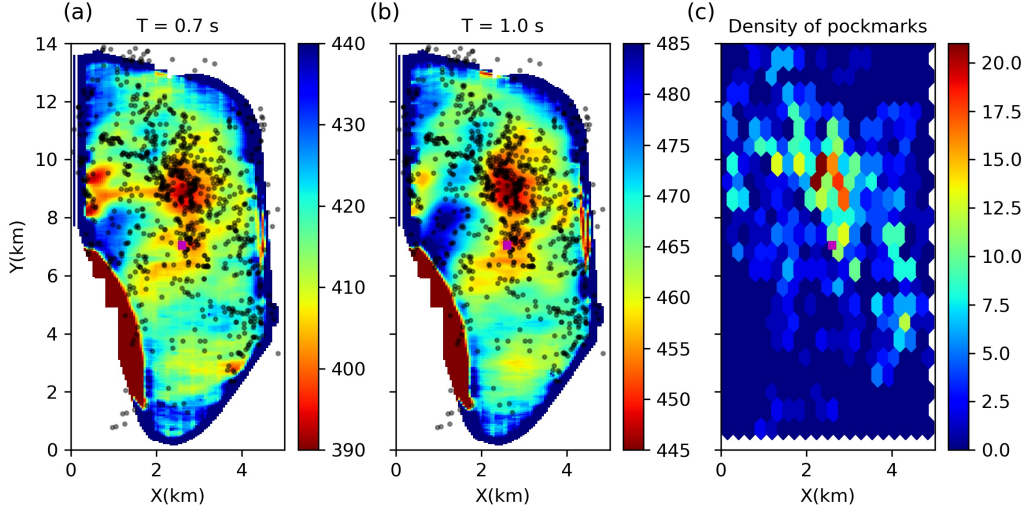


**Figure 8.** Phase velocity maps at (a) 0.7 s and (b) 1.0 s plotted with pockmarks (black dots). (c) The density of pockmark distribution. The magenta rectangle shows the location of the platform.

375 by red solid line box). However, at period 1.6 s though there seems to be some degree  
 376 of similarity in structures with the shorter periods ( $< 1.6$  s), the phase velocity map be-  
 377 comes more complicated. This might due to the poor data quality at longer periods, or  
 378 may be caused by complex structure at greater depths.

379 Overall the uncertainties are low at periods of 1.0 s and 1.3 s ( $\sim 10m/s$ ) and are  
 380 higher at periods of 0.7 s and 1.6 s ( $\sim 25m/s$ ). The high uncertainties at 0.7 s are prob-  
 381 ably caused by the filtering taper at the lower period side (0.67 s - 0.74 s) while the high  
 382 uncertainties at 1.6 s probably indicate higher data uncertainties due to lower SNR since  
 383 phase velocities at longer periods must usually be measured at longer offsets which may  
 384 also partly explain the complex structure in the mean phase velocity map at 1.6 s. Close  
 385 to the boundaries all standard deviation maps show very high uncertainties caused by  
 386 limited data coverage. At the location of the middle low velocity anomaly (blue box),  
 387 the standard deviation map at 0.7 s shows relatively lower uncertainties; this suggests  
 388 that the middle low phase velocity anomaly is probably caused by a low velocity struc-  
 389 ture near to the surface.

390 To better understand the phase velocity maps, we compared the phase velocity map  
 391 at 0.7s and 1.0 s with the distribution of pockmarks at the seabed of Grane field (Fig-

392 ure 8). Pockmarks are craters in the seabed which have been shown to be related to the  
 393 seepage of fluids (gas or liquids) (Kvenvolden, 1989). Figure 8 shows that there is a dense  
 394 distribution of pockmarks at the location of the middle low velocity anomaly from the  
 395 platform to  $Y=11$  km, which suggests that the low velocity anomaly might be caused  
 396 by near surface fluids. At the west edge, the two low velocity anomalies between  $Y=8$   
 397 km and  $Y=10$  km are also consistent with a higher density of pockmark distribution.

398 Figure 9a shows the mean phase velocity maps of the first overtone at the same pe-  
 399 riods as for the fundamental mode. We again outline some noticeable features in the phase  
 400 velocity map at 1 s period. At short periods ( $< 1.6$  s), there is a low velocity anomaly  
 401 at the west edge (blue line box), with a different shape to that observed in the funda-  
 402 mental mode phase velocity maps. This might suggest that this anomaly is caused by  
 403 a change in shape with depth since higher mode phase velocities usually have higher sen-  
 404 sitivities at greater depths compared to fundamental modes. To the north of this low ve-  
 405 locity anomaly there is a low velocity channel at periods of 0.7 s and 1.0 s (red solid line  
 406 box). At the northern edge, a low velocity channel crosses the field from west to east (black  
 407 line box). Similarly, this low velocity channel cannot be clearly observed on the funda-  
 408 mental mode phase velocity maps, which indicates that it might be related to deeper struc-  
 409 ture. In the south of the field there is a similar low velocity anomaly as observed in the  
 410 fundamental mode phase velocity maps (black dashed line box), which may indicate a  
 411 consistent low velocity structure from shallow to deeper levels. Overall, at longer peri-  
 412 ods (i.e. 1.3 s and 1.6 s) the phase velocity maps show very complicated structures as  
 413 we have seen in the fundamental mode phase velocity map at period of 1.6 s. This may  
 414 suggest a complicated deeper structure, or may simply be due to the low quality of data  
 415 at longer periods. Note that the phase velocity maps of the first overtone exhibit much  
 416 shorter scale structure compared to the fundamental model because of lower data qual-  
 417 ity of the first overtone. When these phase velocities are used to invert for shear veloc-  
 418 ities, the shorter scale structure may cause lack of coherence between adjacent 1-D mod-  
 419 els over depth. To reduce this issue, instead of using Eikonal tomography a regularised  
 420 inversion might be used to estimate spatially smoother phase velocity maps.

421 Overall the standard deviation maps of the first overtone show higher uncertain-  
 422 ties compared to the fundamental mode (Figure 9b) due to the fact that the SNR of the  
 423 first overtone is lower than that of the fundamental mode. Similarly to the fundamen-  
 424 tal mode, higher uncertainties are observed at periods of 0.7 s and 1.6 s ( $\sim 100m/s$ ) than

425 at periods of 1 s ( $\sim 50m/s$ ) and 1.3 s ( $\sim 80m/s$ ). The uncertainties are significantly  
 426 smaller between Y=8 km and Y=10 km at periods of 0.7 s and 1.6 s, showing that this  
 427 area is well determined, so the low velocity anomaly at this area (blue line box) is well  
 428 determined. Similarly, there is low uncertainty at the north edge associated with the low  
 429 velocity channel (black line box) and low uncertainty in the south associated with the  
 430 low velocity anomaly (black dashed line box). The standard deviation map at 0.7 s shows  
 431 some higher uncertainty areas ( $\sim 160m/s$ ), e.g., the western edge between Y=10 km  
 432 and Y=12 km and between Y=6 km and Y= 8 km, which is probably caused by low res-  
 433 olution of those areas. Similarly, there is a high uncertainty area between Y=10 km and  
 434 Y=12 km at the west edge at period of 1.6 s.

## 435 5 Shear-wave velocity inversion

436 Although these phase velocity maps can be interpreted for useful information about  
 437 the subsurface, such maps cannot provide good indications of the depths of observed struc-  
 438 tures since Scholte wave phase velocities are a consequence of the velocity structure over  
 439 a range of depths. In order to better understand the subsurface structure it is necessary  
 440 to estimate subsurface shear-velocity structures with depth in a separate inversion. Tra-  
 441 ditionally, a two-step inversion scheme is used to invert for shear-velocity structures where  
 442 we use the above phase velocity maps as data and perform 1D depth inversions indepen-  
 443 dently beneath each geographical location. However, Zhang et al. (2018) used synthetic  
 444 data to show that such a scheme introduces biases in the final 3D shear-velocity struc-  
 445 ture because each of the depth inversions is conducted independently, whereas in real-  
 446 ity they are strongly correlated spatially. Zhang et al. (2018) therefore proposed a fully  
 447 3D Monte Carlo inversion method using a 3D parameterization which preserves these  
 448 correlations.

449 To further understand the limitations of traditional two-step inversion schemes, in  
 450 this section we compare results from the two-step method and the 3D method on real  
 451 data. We use Markov chain Monte Carlo (MCMC) to perform both the 1D depth inver-  
 452 sions and the 3D inversion. To limit the computational cost, we only carried out 1D depth  
 453 inversions along a 2D cross-section (the yellow line in Figure 1). In order to study the  
 454 effects of independent 1D inversions, we also carried out a 2D depth inversion along this  
 455 cross-section using a 2D parameterization and the phase velocities along the profile on  
 456 the above maps as data. This inversion is of interest because it uses the phase velocity

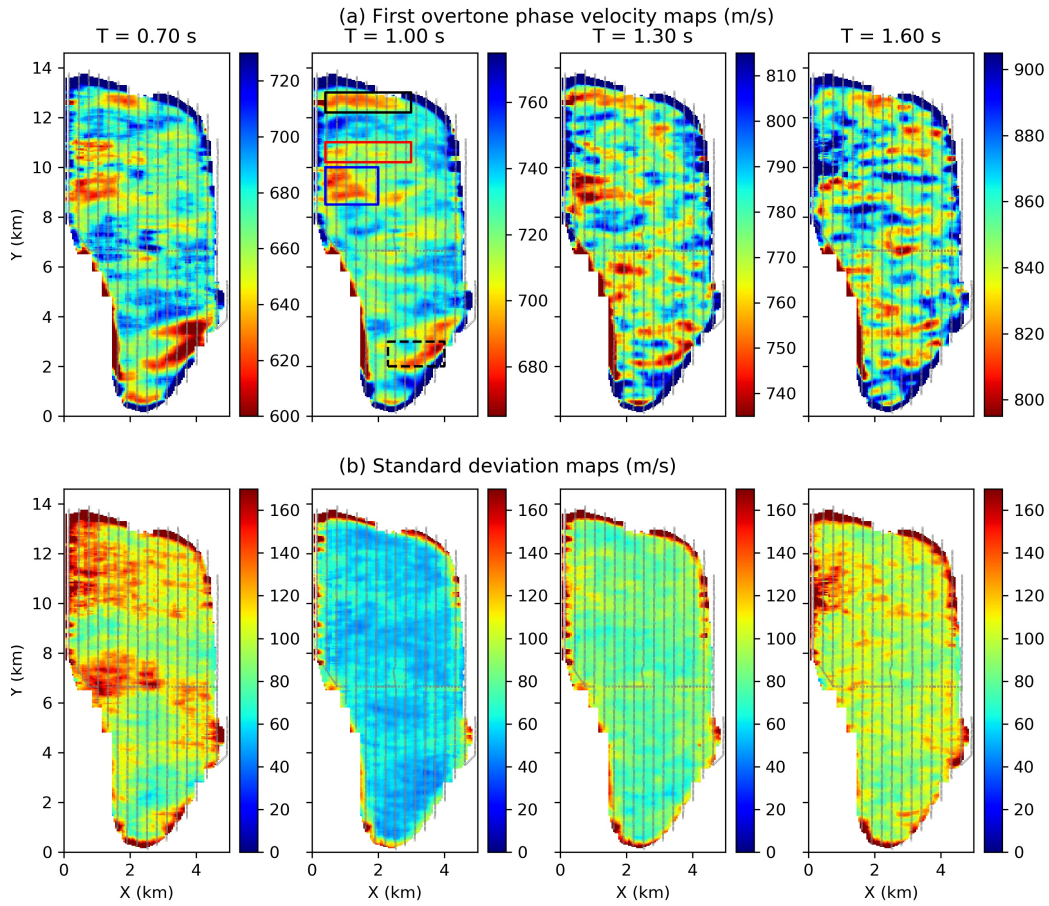


**Figure 9.** (a) Phase velocity maps of the first overtone and (b) their standard deviation maps at periods 0.7s, 1.0s, 1.3s and 1.6s. The boxes in the 1 s period map show locations of features discussed in the text. Gray lines show the distribution of receivers.

457 maps as data similarly to the 1D inversion, but preserves spatial correlations similarly  
 458 to the 3D method. It would therefore be expected a priori to exhibit intermediate per-  
 459 formance compared to the other two methods. In this section, we first describe the two-  
 460 step methods and the 3D method, and then give an overview of the reversible-jump MCMC  
 461 method and the parallel tempering method (which is used to improve computational ef-  
 462 ficiency of MCMC method). We then apply those methods to the Grane data and com-  
 463 pare their results.

## 464 5.1 Methods

### 465 5.1.1 Parameterization

As in Bodin and Sambridge (2009) and Zhang et al. (2018), we use Voronoi tes-  
 sellations to parameterize the subsurface. A Voronoi cell is defined by a point (called a  
 site) and its volume that consists of all of the points nearer to this site than to any other.  
 Figure 10 shows examples of Voronoi tessellations in 1D, 2D and 3D. Each cell contains  
 its location and its properties (e.g., P-wave velocity, shear-wave velocity, density, etc.).  
 Note that in 1D the parametrization with Voronoi cells is inferior to the parametriza-  
 tion with a simple partition model since the same velocity model can be obtained us-  
 ing different configuration of Voronoi cells (Green, 1995). However, for comparison pur-  
 pose in this study we still use a 1D Voronoi parametrization. Since seismic surface waves  
 are primarily sensitive to subsurface shear-wave velocity variations, we only invert for  
 shear-wave velocities. P-wave velocity is linked to the shear-wave velocity via an empir-  
 ical relation (Castagna et al., 1985):

$$V_p = 1.16V_s + 1.36 \quad (10)$$

and density is computed from the P-wave velocity empirically (Brocher, 2005):

$$\rho = 1.74V_p^{0.25} \quad (11)$$

466 where  $V_p$  and  $V_s$  are in  $km/s$ , and density  $\rho$  is in  $g/cm^3$ . Similar to Zhang et al. (2018),  
 467 within each Voronoi cell the velocity is spatially constant.

468 The specific choice of Voronoi parametrization makes it easy to implement in 1D,  
 469 2D and 3D for comparison. At any point in the model, a velocity profile is a layered model  
 470 whose phase or group velocity dispersion curve can be computed using many available  
 471 codes (e.g. Herrmann, 2013) without resorting to approximations. However, while the

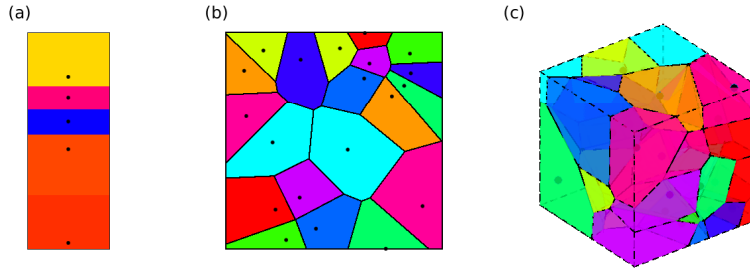


**Figure 10.** Examples of (a) a 1D Voronoi tessellation, (b) a 2D Voronoi tessellation and (c) a 3D Voronoi tessellation of velocity models. Colours represent seismic velocities in each cell. Black dots are the sites that generated each cell.

472 Voronoi parametrization is good at recovery of discontinuities, it can introduce difficul-  
 473 ties to recover a smooth model (Hawkins et al., 2019). The scale length of Voronoi cells  
 474 in higher dimensions can cause models to be distorted and some ad-hoc rescaling is gen-  
 475 erally required (Zhang et al., 2018). It has also been found that Voronoi parametriza-  
 476 tion can produce multi-modalities in the posterior which makes interpretation of uncer-  
 477 tainties difficult. In these cases one could try some other parametrizations, such as wavelets  
 478 (Hawkins & Sambridge, 2015; Dettmer et al., 2016), Johnson-Mehl tessellation (Belhadj  
 479 et al., 2018) and Delaunay and Clouth-Tocher parametrization (Hawkins et al., 2019).

### 480 **5.1.2 2-step inversion**

481 The shear-wave velocity structure is estimated using a 2-step scheme as follows. In  
 482 the first step a series of 2-D phase or group velocity maps for different frequencies are  
 483 estimated tomographically using source-to-receiver or inter-receiver arrival times as data;  
 484 then at each geographical point, the local dispersion curve is used to invert for a 1-D shear  
 485 velocity profile beneath that point. For the first step, either linearised (Nakanishi & An-  
 486 derson, 1983; Trampert & Woodhouse, 1995; Ritzwoller et al., 2002; Snoko & Sambridge,  
 487 2002; Nicolson et al., 2012, 2014) or non-linearised methods (Bodin & Sambridge, 2009;  
 488 Bodin et al., 2012; Khan et al., 2013; Young et al., 2013; Rawlinson et al., 2014; Zulfakriza  
 489 et al., 2014; Saygin et al., 2015; Galetti et al., 2015, 2017; Zheng et al., 2017) can be used

490 to estimate phase or group velocity maps. In this study, since we have a very dense sta-  
 491 tion network, we used Eikonal tomography to determine phase velocity maps (see above).

492 For the second step, we use a non-linear MCMC method to invert for the 1-D shear  
 493 velocity profile beneath each point (Bodin et al., 2012; Young et al., 2013; Galetti et al.,  
 494 2017). Generally those 1D depth inversions are run independently at each geographical  
 495 location without interaction, as this allows perfect parallelisation of what is a compu-  
 496 tationally demanding task. We also carried out a 2D depth inversion along the 2D cross-  
 497 section by using the 2D parameterization described in Figure 10b so as to include lat-  
 498 eral spatial correlations in the inversion. The data used for the 2D inversion is the same  
 499 as those used in the 1D inversions (the local phase velocities from Eikonal tomography).  
 500 For both the 1D and 2D inversions, we used the same forward modelling method, a modal  
 501 approximation method (Herrmann, 2013), to calculate the phase velocity dispersion curves  
 502 from the velocity-versus-depth profiles beneath each geographical point.

### 503 **5.1.3 Fully 3D inversion**

504 In order to determine a 3D shear-velocity model and to be able to compare the three  
 505 different methods (1D, 2D and 3D inversions), we also performed a 3D inversion using  
 506 the 3D MCMC method of Zhang et al. (2018). The subsurface is discretized by Voronoi  
 507 cells (Figure 10c), each of which is defined by the location of its site and its shear-wave  
 508 velocity. As in Zhang et al. (2018), the forward modelling method is an approximate 2-  
 509 step method (Ritzwoller & Levshin, 1998; Stevens et al., 2001; Reiter & Rodi, 2008): first  
 510 a series of phase or group velocity maps at each measurement period are computed by  
 511 extracting the shear velocity profile with depth beneath each geographical point to what  
 512 the 1D modal approximation method of Herrmann (2013) is applied to predict group and  
 513 phase velocities at each period; then for each source-to-receiver or inter-receiver pair, the  
 514 travel times for each period can be determined by tracing rays through the computed  
 515 phase velocity map (for which we use the fast marching method – Rawlinson and Sam-  
 516 bridge (2004)).

517 However, as shown in Galetti et al. (2017), modal approximation methods that are  
 518 usually used (Herrmann, 2013; Saito, 1988) produce unrealistic dispersion curves when  
 519 applied to relatively unusual velocity-depth models. This is due to the fact that these  
 520 methods solve the period equation for the minimum phase velocity solution; unfortunately

521 when the top layer does not have the lowest shear-wave velocity, the dispersion curve with  
 522 minimum phase velocity is likely to be one of the trapped modes generated by a low ve-  
 523 locity layer at depth (Chen, 1993; Wu & Chen, 2016). These trapped modes generally  
 524 oscillate within the low velocity layer, meaning that they cannot actually be observed  
 525 on Earth’s surface and hence do not correspond to forward model using the recorded data.  
 526 Therefore, in order to make the modal approximation modelling package that we used  
 527 (Herrmann, 2013) valid for our inversion, we added a prior constraint on our models –  
 528 that the smallest shear-wave velocity must be in the top layer. The prior is achieved by  
 529 rejecting any proposals of violating models in the Markov chain using a large penalty.  
 530 Note that this choice of prior causes shear velocities at the near surface to prefer small  
 531 values (see Support information, Figure S1). Considering that this is generally thought  
 532 to be true for most of the real Earth, we feel that this is an acceptable and pragmatic  
 533 solution.

#### 534 **5.1.4 Reversible-jump Markov chain Monte Carlo (McMC)**

535 McMC is a class of algorithms that generate a set (or chain) of samples from a tar-  
 536 get probability density (Sivia, 1996). The Metropolis-Hastings algorithm (Metropolis &  
 537 Ulam, 1949; Hastings, 1970) is one such algorithm and was introduced to Geophysics over  
 538 two decades ago (Mosegaard & Tarantola, 1995; Malinverno et al., 2000; Malinverno, 2002;  
 539 Malinverno & Briggs, 2004). In this study, we use a generalised version of the Metropolis-  
 540 Hastings algorithm called reversible jump Markov chain Monte Carlo (rj-McMC) (Green,  
 541 1995; Green & Hastie, 2009). This algorithm allows a trans-dimensional inversion which  
 542 means that the number of model parameters can change along the chain. Thus the pa-  
 543 rameterization of the seismic velocity model can itself be determined by data and prior  
 544 information, avoiding fixing the parameterisation prior to inversion (Bodin & Sambridge,  
 545 2009; Bodin et al., 2012; Young et al., 2013; Galetti et al., 2015, 2017; Hawkins & Sam-  
 546 bridge, 2015; Piana Agostinetti et al., 2015; Burdick & Lekić, 2017; Zhang et al., 2018).  
 547 Note that the specific choice of parametrization (e.g., Voronoi cells) can impose restric-  
 548 tions on models and may affect the final results (Hawkins et al., 2019).

In seismic tomography, the target probability density can be expressed as a Bayesian posterior probability density function (pdf) of the velocity model  $\mathbf{m}$  given the observed

data  $\mathbf{d}_{obs}$ , written  $p(\mathbf{m}|\mathbf{d}_{obs})$ . According to Bayes' theorem,

$$p(\mathbf{m}|\mathbf{d}_{obs}) = \frac{p(\mathbf{d}_{obs}|\mathbf{m})p(\mathbf{m})}{p(\mathbf{d}_{obs})} \quad (12)$$

549 where  $p(\mathbf{d}_{obs}|\mathbf{m})$  is called the *likelihood* and is the probability of observing the measured  
 550 data conditional on a certain model  $\mathbf{m}$  being true,  $p(\mathbf{m})$  describes the prior information  
 551 about model  $\mathbf{m}$  (information that is known independent of data  $\mathbf{d}_{obs}$ ), and  $p(\mathbf{d}_{obs})$  is a  
 552 normalization factor called the *evidence*. We assume a Gaussian data error distribution  
 553 for our likelihood with the data variance as an additional parameter that is also estimated  
 554 during the inversion hierarchically (for more information see Malinverno & Briggs, 2004;  
 555 Bodin et al., 2012; Galetti et al., 2017; Zhang et al., 2018). For the prior pdf we use an  
 556 uninformative prior – a Uniform distribution with wide bounds on the values of each pa-  
 557 rameter.

In the rj-McMC algorithm, a new model  $\mathbf{m}'$  in the chain is drawn from a proposal  
 distribution  $q(\mathbf{m}'|\mathbf{m})$  that depends on the current model  $\mathbf{m}$ , and is accepted or rejected  
 with a probability  $\alpha(\mathbf{m}'|\mathbf{m})$  called the acceptance ratio, given by (Green, 1995)

$$\alpha(\mathbf{m}'|\mathbf{m}) = \min[1, \frac{p(\mathbf{m}')}{p(\mathbf{m})} \times \frac{q(\mathbf{m}|\mathbf{m}')}{q(\mathbf{m}'|\mathbf{m})} \times \frac{p(\mathbf{d}_{obs}|\mathbf{m}')}{p(\mathbf{d}_{obs}|\mathbf{m})} \times |\mathbf{J}|] \quad (13)$$

558 where  $\mathbf{J}$  is the Jacobian matrix of the transformation from  $\mathbf{m}$  to  $\mathbf{m}'$  and is used to ac-  
 559 count for the volume changes of parameter space during jumps between dimensionali-  
 560 ties. In our case, it can be shown that the Jacobian is an identity matrix (Bodin & Sam-  
 561 bridge, 2009). Once a new model is generated via the proposal distribution, it is accepted  
 562 or rejected by generating a random number  $\gamma$  from the uniform distribution on  $[0, 1]$  and  
 563 comparing it with the value of the acceptance ratio  $\alpha$ . If  $\gamma < \alpha$ , the new model is ac-  
 564 cepted; otherwise, the new model is rejected and the current model is repeated as a new  
 565 sample in the chain. The form of the acceptance ratio  $\alpha$  in equation 13 ensures that the  
 566 density of samples in the Markov chain converges to the Bayesian posterior probability  
 567 distribution  $p(\mathbf{m}|\mathbf{d}_{obs})$  as the number of samples tends to infinity (Green 1995).

568 In seismic tomography problems five types of model perturbations are possible: adding  
 569 a new Voronoi cell, removing a cell, moving a cell, changing the velocities and changing  
 570 the data noise hyperparameters. Thus, our algorithm can be described as:

- 571 1. Draw an initial model randomly from the prior pdf.

- 572           2. Generate a new model  $\mathbf{m}'$  by randomly choosing one of the five possible pertur-
- 573           bation types listed above, and then perturbing the current model according to the
- 574           proposal probability.
- 575           3. Calculate the acceptance ratio  $\alpha$  and accept the proposed model to be the new
- 576           sample with probability  $\alpha$ ; otherwise use the current model as the new sample.
- 577           4. Repeat from (ii).

578           We use a Gaussian proposal distribution for the fixed-dimensional perturbations

579           of moving a cell, changing velocities and changing data noise hyperparameters (Bodin

580           & Sambridge, 2009; Zhang et al., 2018). For trans-dimensional perturbations (adding

581           or deleting a cell) we choose to use the prior pdf as the proposal probability since that

582           leads to a higher acceptance ratio compared to using a Gaussian distribution (Dosso et

583           al., 2014; Zhang et al., 2018). It is a property of McMC methods that in principle the

584           choice of proposal distribution does not affect the fact that the final distribution of sam-

585           ples tends to the posterior pdf as the number of samples tends to infinity, although Galetti

586           and Curtis (2018) show that in practice improper Gaussian steps can lead to non-convergence

587           of the chain.

588           To make the ensemble of Markov chains more manageable in size, we only retain

589           every 100th sample of the chain. Monitoring of McMC convergence can be difficult and

590           is always subjective (Green & Hastie, 2009; Bodin & Sambridge, 2009). In this study,

591           we monitored several scalar statistics such as the absolute residual and the number of

592           cells, to diagnose apparent convergence (Bodin & Sambridge, 2009; Hawkins & Sambridge,

593           2015; Piana Agostinetti et al., 2015; Galetti et al., 2017; Zhang et al., 2018). However,

594           we note that this is still an open problem.

### 595           5.1.5 *Parallel tempering*

Parallel tempering is a technique that mixes information between parallel tempered Markov chains to improve efficiency of McMC methods (Earl & Deem, 2005; Dettmer & Dosso, 2012; Dosso et al., 2012; Sambridge, 2013). First, a set of chains are scaled using different temperatures, such that their target probability can be denoted as:

$$\pi(\mathbf{m}|T_i) = p(\mathbf{m}|\mathbf{d})^{1/T_i}, \quad (14)$$

where  $T_i$  is the  $i^{\text{th}}$  temperature,  $p(\mathbf{m}|\mathbf{d})$  is the posterior probability density and  $\pi(\mathbf{m}|T_i)$  is called the tempered posterior pdf. Those tempered Markov chains are then run in parallel. Models can be swapped between chains randomly based on an acceptance ratio called detailed balance (Earl & Deem, 2005; Sambridge, 2013):

$$\alpha(i, j) = \min\left\{1, \left[\frac{p(\mathbf{m}_j|\mathbf{d})}{p(\mathbf{m}_i|\mathbf{d})}\right]^{1/T_i} \left[\frac{p(\mathbf{m}_i|\mathbf{d})}{p(\mathbf{m}_j|\mathbf{d})}\right]^{1/T_j}\right\}, \quad (15)$$

596 where  $\alpha(i, j)$  is the acceptance ratio of a swap between model  $\mathbf{m}_i$  and  $\mathbf{m}_j$  at tempera-  
 597 ture  $T_i$  and  $T_j$ , respectively. By doing so, one can sample the combined posterior dis-  
 598 tribution  $\pi(\mathbf{m}|T_i)$ , ( $i = 1, \dots, n$ ). At higher temperatures the posterior probability den-  
 599 sity function becomes flatter, which improves the ability of McMC to escape local min-  
 600 ima and to explore parameter space more globally. By enabling exchange between dif-  
 601 ferent temperatures, the method thus improves the explorative performance of the Markov  
 602 chain at  $T = 1$ , which (still) samples our target posterior probability.

The choice of temperature ladder of the parallel chains strongly affects the efficiency of parallel tempering. It has been shown that a power-law temperature schedule is generally more efficient than a uniformly distributed schedule (Calderhead & Girolami, 2009; Sengupta et al., 2015), so here we used a power-law schedule. Given a total of  $N$  chains, the temperatures can be distributed as:

$$1/T_i = 1 - \left(\frac{i}{N}\right)^p, \quad (16)$$

603 where  $T_i$  is the  $i^{\text{th}}$  temperature and  $p$  is the power coefficient which can be chosen ac-  
 604 cordingly. To reduce the overhead introduced by synchronization and communication  
 605 of parallel chains, we only swap models every 50th iteration.

Usually only samples from those chains with  $T = 1$  are stored for later inference (Sambridge, 2013; Ray et al., 2017; Galetti & Curtis, 2018). However, for sophisticated problems, parallel tempering often demands a large number of tempered chains to improve the efficiency of McMC methods, which leads to a high computational cost. Those chains with  $T > 1$  can also be used for Bayesian inference via an importance resampling scheme (Geyer, 1994; Dosso et al., 2012). Suppose that we have samples from an unnormalized density  $h$  and want to calculate an integration with respect to another unnormalized density  $h_\theta$ . This is important since most of the statistics that we usually wish to calculate (the mean model, variance, etc.) are integrals. Such integrals can be com-

puted by using the importance sampling formula as weighted averages:

$$E_{\theta}g(X) = \sum_{j=1}^n w_{\theta}(X_j)g(X_j) \quad (17)$$

where  $\theta$  denotes that the expectation is calculated with respect to probability density  $h_{\theta}$ ,  $g$  is the function of which we want to calculate expectation, and

$$w_{\theta}(x) = \frac{h_{\theta}(x)/h(x)}{\sum_{j=1}^n h_{\theta}(X_j)/h(X_j)} \quad (18)$$

Substituting  $h_{\theta}(x)$  with  $\pi(\mathbf{m}|T_0)$ , and  $h(x)$  with  $\pi(\mathbf{m}|T_i)$ , the weight  $w_{T_0}(\mathbf{m})$  can be expressed as:

$$w_{T_0}(\mathbf{m}) = \frac{\pi(\mathbf{m}|T_0)/\pi(\mathbf{m}|T_i)}{\sum_{j=1}^n \pi(\mathbf{m}_j|T_0)/\pi(\mathbf{m}_j|T_i)} \quad (19)$$

where  $\mathbf{m}_j$  is the  $j^{th}$  sample from the chain with  $T = T_i$ ,  $T_0 = 1$ , and  $\pi(\mathbf{m}|T_0)$  is the density in which we are interested. Combining equation (19) with equation (14),  $w_{T_0}$  will be:

$$w_{T_0}(\mathbf{m}) = \frac{\pi(\mathbf{m})^{1-\frac{1}{T_i}}}{\sum_{j=1}^n \pi(\mathbf{m}_j)^{1-\frac{1}{T_i}}} \quad (20)$$

606 where  $\pi(\mathbf{m}) = p(\mathbf{m}|\mathbf{d})$  is the target posterior at  $T = 1$ . Using this equation and equa-  
 607 tion (17), one can calculate any expectations using samples from the tempered chain with  
 608  $T = T_i$  with respect to the target density  $\pi(\mathbf{m})$ .

## 609 5.2 Application to Grane field

610 We applied the above suite of methods to the Grane field data to estimate shear-  
 611 wave velocity structures and compared the results. In this section, we used phase veloc-  
 612 ity dispersion data of fundamental mode Rayleigh-type Scholte waves to invert for the  
 613 shear-wave velocity structure. For two-step inversions (the 1D and 2D inversions described  
 614 above) we extracted those local phase velocities that lie along the top of a 2D cross-section  
 615 (see Figure 1) from the phase velocity maps. This produces 257 dispersion curves, one  
 616 for each geographical location (Figure 11). Since the computational cost scales with the  
 617 minimum of the number of virtual sources and receivers, for the 3D inversion we only  
 618 used a subset of 36 receivers as virtual sources (Figure 12a), each recorded on all 3458  
 619 receivers, and picked phase velocities for each virtual source-to-receiver pair. This gener-  
 620 erates 41842 dispersion curves which constitutes our 3D inversion dataset. Figure 12b  
 621 shows a density map of straight ray paths for those picked phase velocities at 1.0 s. Sim-  
 622 ilarly to the above phase velocity tomography, we only used periods from 0.7 s to 2.0 s  
 623 with a spacing of 0.1 s (Figure 12c).

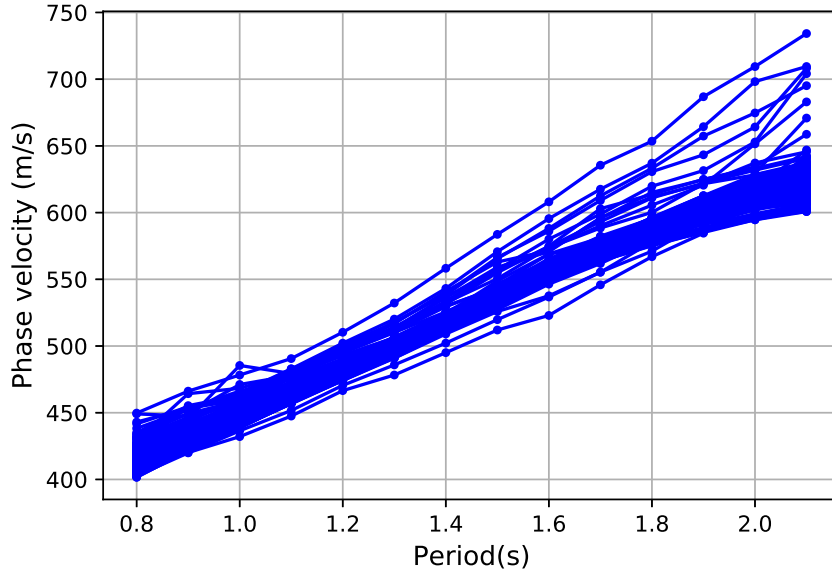


**Figure 11.** Local phase velocity dispersion curves at points along a 2D cross-section (yellow line in Figure 1) extracted from phase velocity maps. These were used as data for our two-step inversions (1D and 2D inversions).

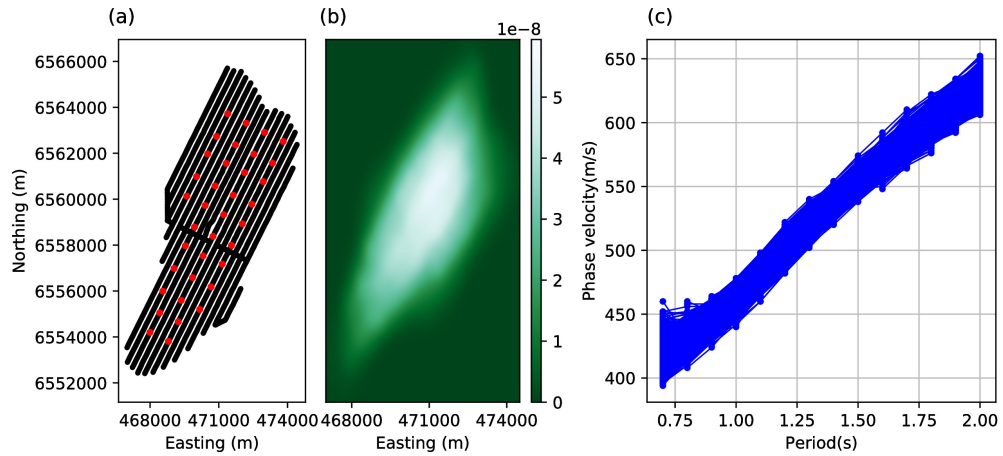


**Figure 12.** (a) Receivers used as virtual sources (red dots) for the 3D inversion. Phase velocity dispersion curves are picked from those virtual sources to all 3458 receivers. (b) Density of ray paths of phase velocity at 1.0 s and (c) phase velocity (travel time) dispersion curves.

624 For 1D depth inversions, the prior pdf of the number of layers is chosen to be a dis-  
625 crete uniform distribution between 2 and 20 layers and the prior of shear velocity is set  
626 to be a uniform distribution between 200 m/s and 1400 m/s. The noise level of the like-  
627 lihood is parameterized using a hyperparameter  $\gamma$  which serves as a scaling factor of a  
628 prior Gaussian uncertainty that has standard deviation which comes from the results of  
629 Eikonal tomography above (Galetti et al., 2017). The prior of this hyperparameter is sim-  
630 ply chosen to be a uniform distribution between 0.001 and 1.0. Since the sea floor depth  
631 varies smoothly across Grane field, we assumed an averaged water depth of 127 m ev-  
632 erywhere. For the proposal distribution we use a Gaussian distribution: the width of the  
633 Gaussian for fixed-dimensional steps (velocity change, moving a cell site and hyperpa-  
634 rameter change) is chosen by trial and error to ensure the acceptance ratio is between  
635 20 and 50 percent (Hawkins & Sambridge, 2015; Zhang et al., 2018); the width for the  
636 trans-dimensional step (birth and death) is selected to produce the maximum possible  
637 acceptance ratio. For each inversion at each geographical location we used eight chains,  
638 and each chain is run for 3,000,000 iterations with a burn-in period of 1,000,000 during  
639 which all samples are ignored for subsequent inference of the posterior pdf. Each chain  
640 is thinned by retaining every 100th sample after burn-in, and those samples are used to  
641 estimate the posterior pdf's mean and standard deviation.

642 For the 2D inversion we used a discrete uniform distribution between 100 and 400  
643 as the prior on the number of cells, and the same prior distribution for shear velocity as  
644 in 1D inversions. For the noise parameterization we used only one hyperparameter for  
645 each period across the section as a scaling factor for uncertainties from Eikonal tomog-  
646 raphy. Thus we maintain the relative uncertainty structures from Eikonal tomography  
647 across the 2D section. The prior for this hyperparameter is chosen to be a uniform dis-  
648 tribution between 0.01 and 1. Similarly to above, the proposal distribution for fixed-dimensional  
649 steps (velocity change, moving a cell, hyperparameter change) is selected to give an ac-  
650 ceptance ratio between 20 and 50 percent. For the trans-dimensional step (birth and death)  
651 we used the prior pdf as the proposal distribution (Dosso et al., 2014; Zhang et al., 2018).  
652 As shown in Zhang et al. (2018), the high lateral-to-vertical spatial aspect ratio fo the  
653 cross-section can affect the efficiency of MCMC sampling when using Voronoi cells. There-  
654 fore, we applied a scaling factor of 8 for the vertical dimension to reduce the aspect ra-  
655 tio. We used a total of 16 chains for the 2D inversion and collected 4,000,000 samples

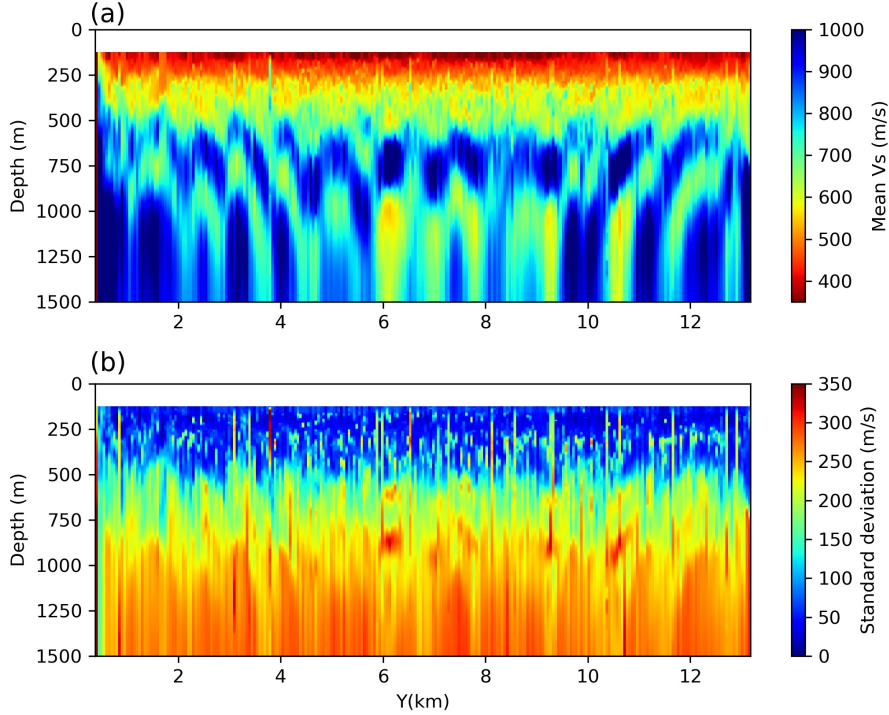


**Figure 13.** (a) Mean and (b) standard deviation of shear velocity  $V_s$  along the 2D cross-section (see Figure 1) from independent 1D Monte Carlo depth inversions. The white top layer represents the water layer which has zero shear velocity.

656 from each chain with a burn-in period of 2,000,000. Each chain is thinned by a factor  
 657 of 100.

658 For the 3D inversion, the prior of the number of cells is set to be a discrete uni-  
 659 form distribution between 400 and 1500 since the Grane field has a relatively complex  
 660 structure as indicated by the complex phase velocity maps. We used the same prior for  
 661 the shear velocity as in 1D and 2D inversions. The noise level is derived from two pa-  
 662 rameters  $\sigma_0$  and  $\sigma_1$  using equation  $\sigma = \sigma_0 * traveltime + \sigma_1$  as in Zhang et al. (2018).  
 663 The prior density of the two noise hyperparameters are set to be a uniform distribution  
 664 between 0.0001 and 0.02 and a uniform distribution between 0.0 and 0.1, respectively.  
 665 The proposal distribution for fixed-dimensional steps are chosen in a similar way to those  
 666 in the 1D and 2D inversions. For trans-dimensional steps the prior is used as the pro-  
 667 posal distribution. As in the 2D inversion, the vertical aspect ratio is scaled by 8 to com-  
 668 pensate for the high lateral-to-vertical difference in scaling. To improve the efficiency of

669 3D McMC we applied parallel tempering. A total of 24 chains are used with 16 chains  
 670 at temperature 1. The temperatures of the other chains are chosen using equation (16)  
 671 with  $p = 3$  and  $N = 8$ . For each chain we generated 2,700,000 samples with a burn-  
 672 in period of 1,000,000 and maintained only every 100th sample after burn-in.

### 673 5.3 Results of shear velocity tomography

674 Figure 13 shows the shear-velocity mean and standard deviation from 1D inver-  
 675 sions. In the near surface ( $< 250$  m), the model has a relatively low velocity layer ( $\sim 400$   
 676 m/s, see Figure 16a). Between 250 m and 600 m the velocity is slightly higher ( $\sim 650$   
 677 m/s) and shows complicated structures which are likely caused by the independence of  
 678 each 1D inversion. This latter effect is also reflected by some laterally sharp discontinu-  
 679 ities across the section. Below 600 m the model shows a high velocity layer ( $\sim 900$  m/s)  
 680 between  $Y=6$  km and  $Y=9.5$  km down to 800 m. At each side ( $Y < 6$  km and  $Y > 9.5$   
 681 km), parallel, dipping, alternating high and low velocity anomalies are observed across  
 682 the section. At the bottom ( $> 800$  m) there exists alternating vertical high and low ve-  
 683 locity anomalies. These high and low velocity anomalies are possibly related to similar  
 684 structures observed in the phase velocity maps at longer periods (Figures 7 and 9). How-  
 685 ever, due to high uncertainties ( $> 200$  m/s) at greater depths ( $> 600$  m, see Figure 16)  
 686 , those complicated structures are probably not interpretable. The standard deviation  
 687 map (Figure 13b) shows that the near surface structure ( $< 500$  m) is apparently well con-  
 688 strained since surface waves are more sensitive to shallower depths (Figure 16a). Note  
 689 however that there are also lateral discontinuities in the uncertainty map caused by the  
 690 independence of each 1D inversion; these generally show that the corresponding phase  
 691 velocity discontinuities are not well resolved (they have very high uncertainty). Note that  
 692 in this study the phase velocity maps are obtained using Eikonal tomography in which  
 693 no explicit regularization is imposed. As a result the phase velocity maps show some short-  
 694 scale structures which may cause some roughness in the shear velocity model estimated  
 695 by independent 1D inversions. To reduce this issue the conventional regularized tomog-  
 696 raphy may be used to produce smoother phase velocity maps, and consequently to pro-  
 697 duce a smoother shear velocity model.

698 For comparison, Figure 14 shows the results from the 2D inversion. Overall the mean  
 699 velocity model is smoother because of lateral interactions that are included in the 2D  
 700 parameterization. The near surface structure is generally similar to that from 1D inver-

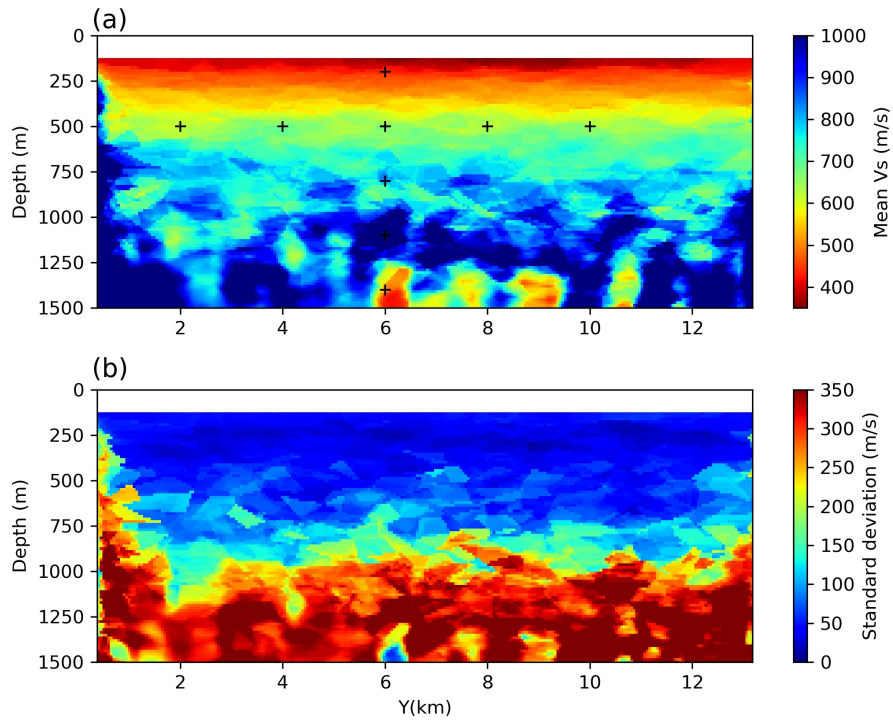


**Figure 14.** (a) Mean and (b) standard deviation of shear velocity along the 2D cross-section (see Figure 1) from the 2D Monte Carlo inversions. The white top layer represents the water layer which has zero shear velocity. Black pluses indicate locations of which marginal distributions are shown in Figure S3 in support information.

701 sions: a low velocity layer at depths  $< 250$  m. However, between 250 m and 600 m, the  
 702 2D result shows far smoother structures compared to the discontinuous structures in the  
 703 1D result. Below 600 m the two results show very different structures. Instead of the clear  
 704 high velocity anomalies and dipping structures that appeared between 600 m and 800  
 705 m in the 1D result, the 2D result exhibits smoother structures. Below 800 m the struc-  
 706 ture becomes more complicated and at greater depths ( $> 1000$  m) we also observe some  
 707 vertical high and low velocity anomalies similar to the 1D results. The standard devi-  
 708 ation map shows that uncertainties are relatively small ( $< 100$  m/s) from the surface down  
 709 to 800 m (Figure 16b), which is significantly deeper than for the 1D inversions (500 m).  
 710 This is probably because by including lateral spatial correlations, and because the near  
 711 surface structure is better determined which further improves the resolution at greater  
 712 depths. Below 800 m we have very high standard deviations ( $\sim 350$  m/s) as expected.

713 Note that in the 2D results, there are artefacts caused by Voronoi cells at greater  
 714 depths ( $> 500$  m). To evaluate convergence of Markov chains, Figure S2 in the support-  
 715 ing information shows the history of misfits and averaged noise level, and the histogram  
 716 of number of cells. We also show marginal distributions of shear velocity at points in the  
 717 cross section (black pluses in Figure 14) in Figure S3. To further study the convergence  
 718 and the results of the 2D inversion, we conducted another independent inversion with  
 719 the same number of chains and the same number of samples as in the previous 2D in-  
 720 version. The results (Figure S4 in the supporting information) show similar results to  
 721 those in the previous 2D results. We therefore conclude that the 2D Markov chains have  
 722 almost converged. However, because errors in the phase velocity maps obtained using  
 723 Eikonal tomography may produce a complex posterior distribution of shear velocity mod-  
 724 els, it is certainly possible that Markov chains got stuck at local modes. This may be  
 725 the reason for the Voronoi cell shaped artefacts.

726 Note that there is a low velocity anomaly with small standard deviations at  $Y=6$   
 727 km at the bottom of the cross section, which also exists in the 1D inversion results (Fig-  
 728 ure 13) and in another 2D inversion result (Figure S4). Therefore the anomaly may be  
 729 caused by errors in the phase velocity maps which requires a low velocity value at greater  
 730 depths. Since the bottom layer of models are assumed to be a half-space, these aggre-  
 731 gated the resolution of velocity at all greater depths, which explains why the anomaly  
 732 shows a low standard deviation (this is a common problem for such trans-dimensional  
 733 depth inversion – see Zhang et al., 2018). Note that smoother velocity and uncertainty

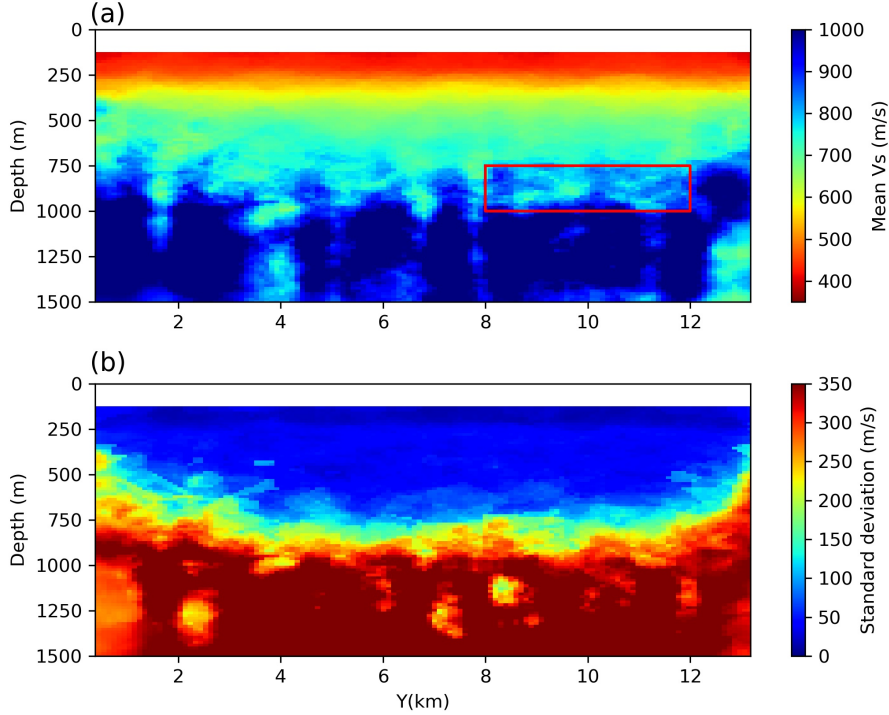


**Figure 15.** (a) Mean and (b) standard deviation of shear velocity along the 2D cross-section (see Figure 1) from the 3D Monte Carlo inversion. The white top layer represents the water layer which has zero shear velocity.

734 models can be obtained by explicitly smoothing the results (Young et al., 2013; Chmiel  
 735 et al., 2019). For fair comparison of our various models, and to try to avoid ad hoc steps  
 736 in processing we do not apply any smoothing in this study.

737 We show the results from the 3D inversion in Figure 15. In the near surface ( $< 250$   
 738 m) the structure is very similar to the 2D result, showing a clear low velocity layer (Fig-  
 739 ure 16c). Between 250 m and 800 m the structure is smoother compared to both the 2D  
 740 and 1D results, and does not show the high velocity anomalies and dipping structures  
 741 that exist in the 1D result. Around 800 m there is a possible high velocity layer from  
 742  $Y=8$  km to  $Y=12$  km and beneath it there are some isolated low velocity anomalies at  
 743 around 1000 m depth (red box in Figure 15). At the west ( $Y < 8$  km), the model shows  
 744 some high and low velocity anomalies between 800 m and 1000 m. Though the struc-  
 745 ture beneath 1000 m is relatively smooth and shows high velocities ( $> 900$  m/s), there  
 746 are still some vertical structures similar to those in the 2D and 1D results. This suggests

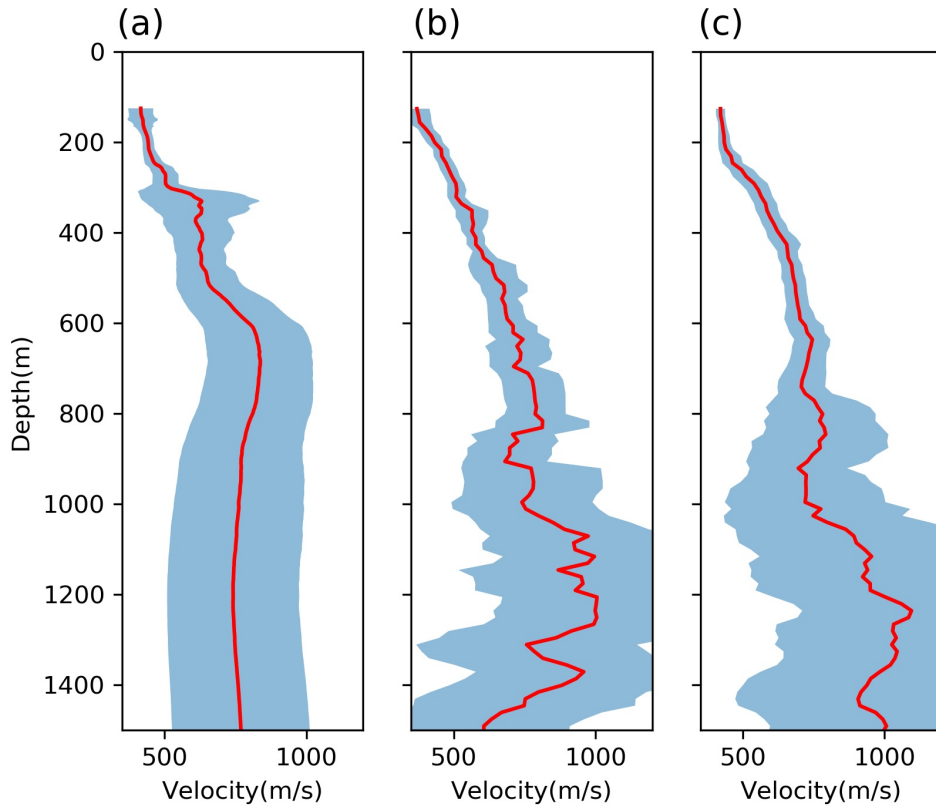


**Figure 16.** 1D marginal mean (red line) and standard deviation (blue area) at the middle ( $Y=6.7$  km) of the 2D cross-section ( see Figure 1) obtained using (a) the 1D Monte Carlo inversion, (b) the 2D Monte Carlo inversion and (c) the 3D Monte Carlo inversion.

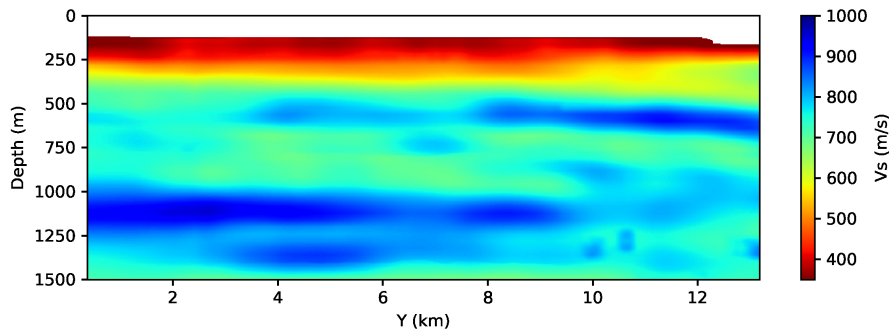


**Figure 17.** Shear-wave velocity  $V_s$  model from reflection tomography obtained using active source seismic data. The white top layer represents the water layer which has zero shear velocity.

747 that these structures are probably related to the similar structures in the phase veloc-  
748 ity maps and might indicate useful information about the subsurface, or may be caused  
749 by poor quality data at longer periods. Similarly to the 2D results, we have low uncer-  
750 tainties from the surface down to 800 m (Figure 16c). Therefore, by including lateral spa-  
751 tial correlations in the 2D and 3D inversions, we can have greater confidence at larger  
752 depths than in the 1D inversion. Compared to the 2D uncertainty result, the 3D result  
753 shows lower uncertainties between 400 m and 800 m (Figure 16b and c), and they are  
754 also spatially smoother. This difference might be caused by errors introduced in the phase  
755 velocity maps in the initial 2D Eikonal tomography step (Zhang et al., 2018) since this  
756 produces the data used in the 2D MCMC inversion. Due to the fact that surface waves  
757 are mainly sensitive to the near surface structure, small errors in the phase velocity maps  
758 will affect the deeper structure more than the shallow structure – it might be that large  
759 velocity variations at greater depths are needed to fit biased data. This may also be the  
760 reason why the results of 2D and 3D inversions show different results at depth: since the  
761 3D inversion uses the phase velocity travel time picks directly, it naturally avoids any  
762 errors in the phase velocity maps (Zhang et al., 2018). Note that the two sides of the cross-  
763 section have higher uncertainties which is caused by lower ray path coverage at the two  
764 sides (Figure 15b).

765 To further validate our results and to better understand the three methods, we com-  
766 pare the results with the shear-wave velocity model in Figure 17 which was derived from  
767 PP-PS simultaneous joint tomography using active source seismic data (Bullock et al.,  
768 2015). Overall, the PP-PS tomography model is smoother compared to those from am-  
769 bient noise dispersion inversions, which might be caused by regularization in the PP-PS  
770 tomography (which is not added explicitly in the MCMC inversion). In the near surface  
771 ( $< 400$  m), the PP-PS tomography model is very similar to the results from 2D and 3D  
772 inversions which again suggests that including lateral spatial correlations in the inver-  
773 sion solution improves results. Between 400 and 800 m the PP-PS tomography model  
774 shows a high velocity layer around 500 m, which cannot be observed in any of the three  
775 models from surface wave dispersion inversion. This is probably because that the fre-  
776 quency content of the two inversion are very different and small scale anomalies present  
777 in the PP-PS tomography are unlikely to be resolvable by Scholte wave data. Below 800  
778 m, the PP-PS tomography model is much smoother and does not show the relatively com-  
779 plicated structures of the 2D and 3D results. However even though we have limited res-

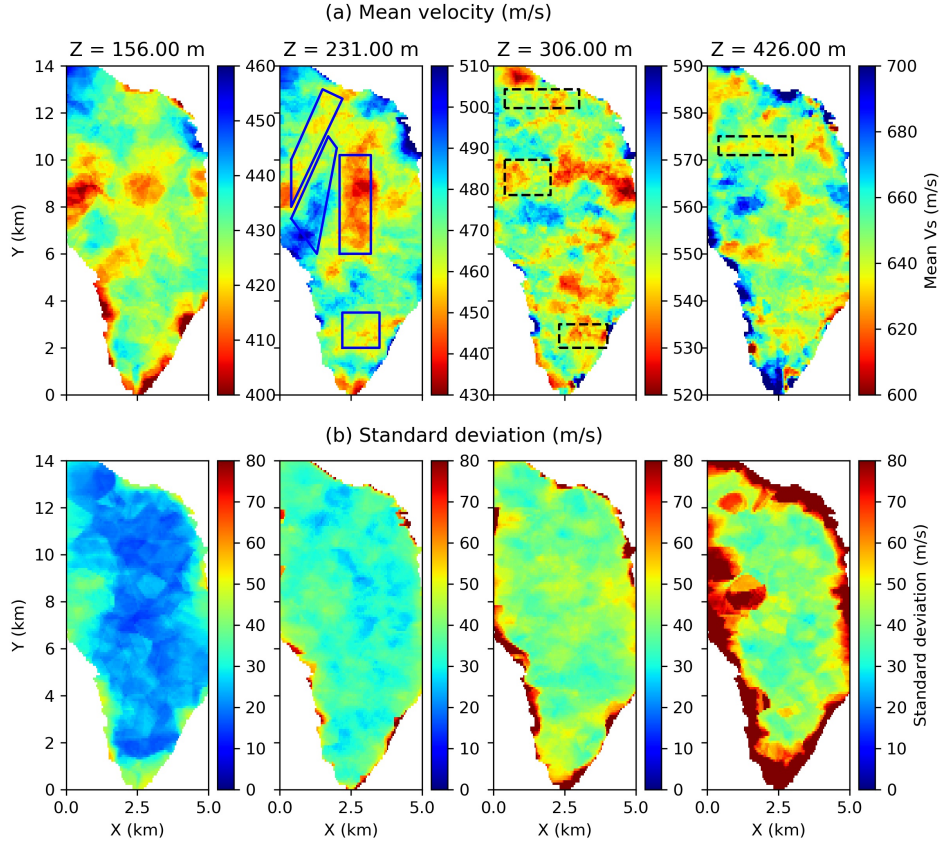


**Figure 18.** Horizontal slices of (a) the mean and (b) standard deviation of the shear velocity model from 3D Monte Carlo inversion at depths of 156 m, 231 m, 306 m and 426 m from left to right across the figure.

780 olution below 800 m, there still seems to be some similarities in the PP-PS tomography  
 781 model and the 3D results, e.g. higher velocities below 1000 m and relatively smoother  
 782 structure compared to the 1D and 2D results. In conclusion, the 3D inversion seems to  
 783 produce a shear-velocity model that is more consistent with PP-PS tomography than  
 784 do 1D and 2D inversions. Note also that the frequency range used in this study is lim-  
 785 ited to 0.7-2.0 Hz, and we only used fundamental mode surface waves. If we use a larger  
 786 frequency range and include higher mode data, the results may be improved further.

787 Figure 18 shows horizontal slices of the pointwise mean and standard deviation of  
 788 the 3D shear velocity model estimated using the 3D Monte Carlo method at depths of  
 789 156 m, 231 m, 306 m and 426 m. The blue line boxes denote the locations of features

790 in the fundamental mode phase velocity maps discussed above, and the black dashed-  
 791 line boxes show the locations of features discussed about the phase velocity maps of the  
 792 first overtone. In the near surface ( $< 250$  m) the shear velocity model has similar struc-  
 793 tures to those in the fundamental mode phase velocity maps at short periods, for exam-  
 794 ple the central low velocity anomaly which might be caused by near surface fluids and  
 795 the low velocity anomaly in the south. This suggests that the phase velocities at short  
 796 periods are mostly determined by the near surface structure. Due to possible interpo-  
 797 lation errors in the Eikonal tomography step, the edges of phase velocity maps are not  
 798 as well determined as in the shear velocity model, which is probably the reason why the  
 799 low velocity anomaly and the high velocity anomaly in the northwest are extended in  
 800 the shear velocity model compared to the phase velocity maps. In the deeper part ( $>$   
 801  $250$  m), as in the phase velocity maps at longer periods, the velocity structures are more  
 802 complicated than in the shallow part. However, although the phase velocity maps of the  
 803 fundamental mode and the first overtone show completely different structures, the shear-  
 804 velocity model inverted using only the fundamental mode indicates some similar features  
 805 as observed in the first overtone phase velocity maps (black dashed-line boxes in Figure  
 806 18). For example, at the depth of  $306$  m there is a low velocity anomaly at the western  
 807 edge between  $Y=8$  km and  $Y=10$  km and a low velocity anomaly at the south around  
 808  $Y=2$  km which also appear in the first overtone phase velocity maps. The low velocity  
 809 channel existing in the first overtone phase velocity maps (red line box in Figure 9) can  
 810 also be clearly observed at a depth of  $426$  m in the shear-velocity model. This further  
 811 suggests that the complicated features in the phase velocity maps at longer periods could  
 812 provide useful information about the subsurface.

813 At the depth of  $306$  m there is a low velocity channel feature between  $Y=3.5$  km  
 814 and  $Y=7.5$  km (black box in Figure 19). This channel-like feature indicates the presence  
 815 of a possible palaeoriver channel at the seabed. Note that this feature cannot be observed  
 816 in either fundamental mode or first overtone phase velocity maps. This suggests that the  
 817 feature might be averaged out in phase velocity maps since phase velocities are a con-  
 818 sequence of structures over a range of depths, a process that our inversion procedures  
 819 are designed to undo.

820 Overall the standard deviation maps suggest relatively low uncertainties ( $< 50$  m/s)  
 821 at all depths, and uncertainties generally increase with depth due to the fact that sur-  
 822 face waves have lower sensitivities at greater depth. The standard deviation map at the

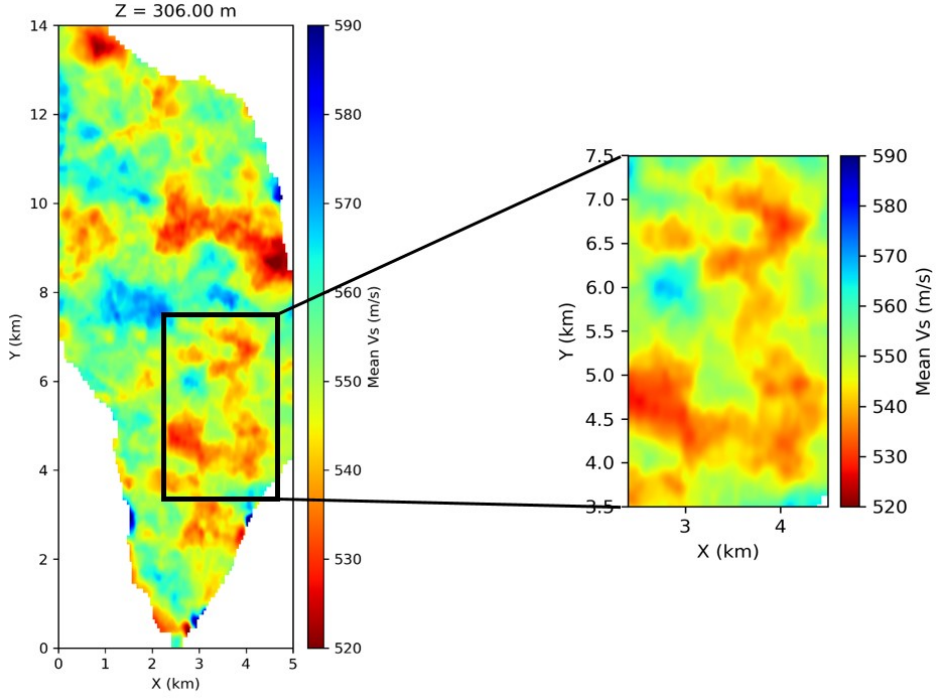


**Figure 19.** The Horizontal slice at depth of 306 m with a detailed structure highlighted in the magnified plot.

823 depth of 231 m shows relatively lower uncertainties at the locations of the velocity anom-  
 824 alies outlined by blue boxes, suggesting that these features are well determined. However,  
 825 due to the insufficient data coverage at the edges, there is a relatively higher uncertainty  
 826 area at the western edge around Y=8 km at the depth of 156 m associated with a low  
 827 velocity anomaly. Similarly, at the western edge between Y=8 km and Y= 10 km the  
 828 standard deviation map at a depth of 426 m shows high uncertainties.

829 **5.4 Analysis of noise level**

830 In this study the data noise level is estimated within the McMC method. Tomo-  
 831 graphic results are generally sensitive to the noise level as it directly affects the complex-  
 832 ity of the model that is needed to fit the data adequately (Bodin et al., 2012). Figure  
 833 20 shows examples of the data noise level at periods of 0.7 s, 1.0 s, 1.3 s and 1.6 s esti-  
 834 mated using the three inversion methods. Figure 20a, b show the noise distribution of  
 835 all of the local phase velocities estimated using the mean scaling factor for the 1D and  
 836 2D inversion respectively, and Figure 20c shows the noise distribution of all of the used

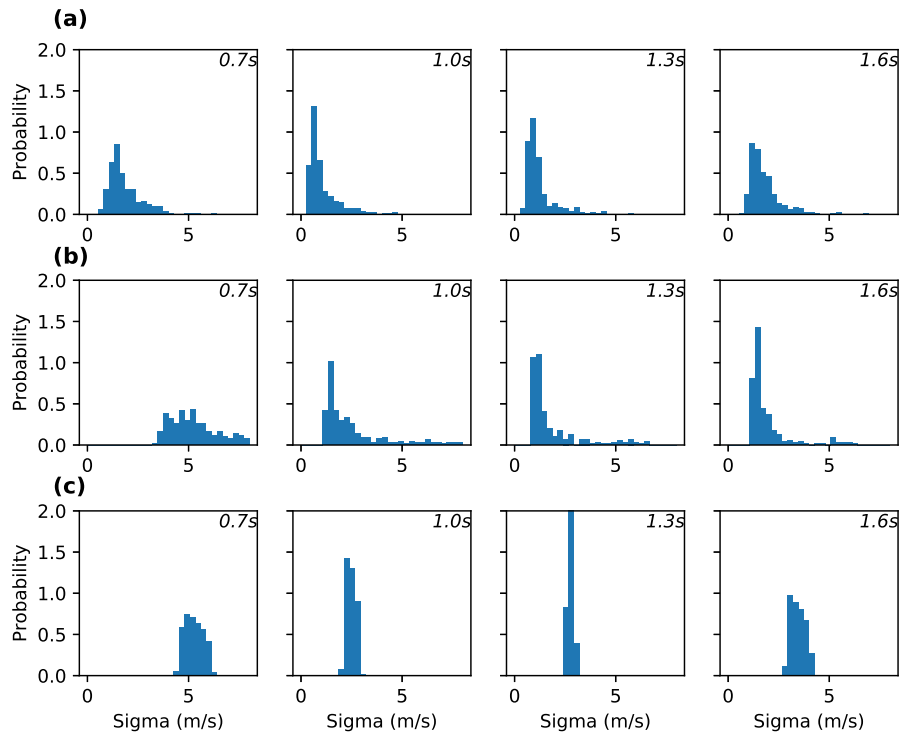


**Figure 20.** Noise distribution of phase velocities from the (a) 1D, (b) 2D and (c) 3D inversions. For each case the distribution is shown at periods of 0.7 s, 1.0 s, 1.3 s and 1.6 s from left to right.

837 phase velocities in the 3D inversion estimated using the mean hyperparameters. Note  
838 that the noise estimated in the 3D inversion is different from those in the 1D and 2D in-  
839 version – the 3D inversion estimates the noise level of travel times between each source-  
840 receiver pair; this is transformed to noise on velocities using straight-ray source-to-receiver  
841 distances. Overall the noise level from the three methods are relatively consistent with  
842 each other – all of them are around 2 to 4 m/s. The noise levels from the 3D inversion  
843 are slightly higher than those from the 1D and 2D inversion since they are essentially  
844 different quantities. The noise estimated from the 1D and 2D inversions are highly con-  
845 sistent, except at the shortest period of 0.7 s. However, from the Eikonal tomography  
846 we observed that the phase velocity map at 0.7 s itself has higher uncertainties than the  
847 others. Therefore it is possible that the 1D inversion overestimated the noise level since  
848 the method might also account for consistency with the prior range of models (Zhang  
849 et al., 2018).

850 To better understand the effects of the noise level on results, we performed the 1D  
851 inversions by fixing the noise level at that estimated using Eikonal tomography (Figure  
852 21). Though there are still some discontinuities in the results due to the independence  
853 of each 1D inversion, this cross-section has a smoother structure than that in Figure13  
854 and does not show the complicated and dipping structures observed previously. How-  
855 ever, by doing this we inevitably sacrifice the resolution at greater depths. For exam-  
856 ple, below 550 m the velocity model is simply equal to the prior. Therefore, the hierar-  
857 chical Bayesian inversion runs the risk of overfitting data for 1D inversions, while a fixed  
858 improper noise estimate might lose resolution (Bodin et al., 2012). In 1D inversions, the  
859 model is generally determined by data at tens of discrete frequency points, which might  
860 lead the inversion problem to be under-determined when complex models are used. As  
861 a result, the MCMC result is very sensitive to the noise level since that determines the  
862 complexity of the model.

863 To better constrain the model, we carried out another inversion including the first  
864 overtone dispersion data (Figure 22). The noise level is fixed at the uncertainties esti-  
865 mated using Eikonal tomography. The mean velocity model (Figure 22a) has fewer dis-  
866 continuities than the result from inversion using only the fundamental mode, and the  
867 layer boundaries are also better constrained in depth. The standard deviation model (Fig-  
868 ure 22b) shows that the near surface layer has smaller uncertainties compared to the pre-  
869 vious result. At deeper levels (500 - 700 m), the model is also better determined since

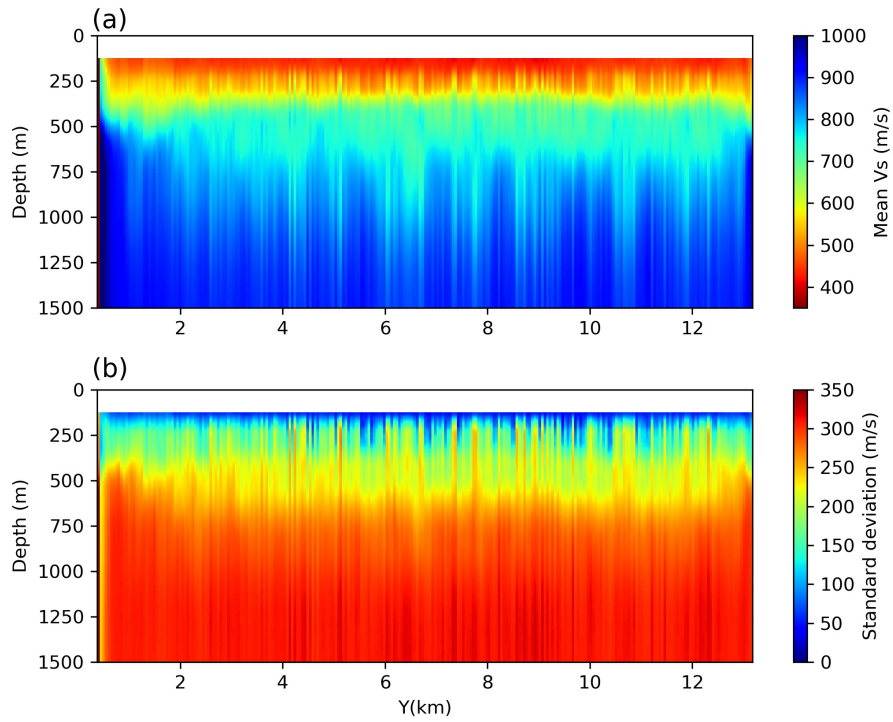


**Figure 21.** (a) Mean and (b) standard deviation of shear velocity  $V_s$  from independent 1D Monte Carlo inversions using only fundamental mode Rayleigh-type Scholte wave phase velocities with noise levels fixed to be uncertainties estimated from Eikonal tomography. The white top layer represents the water layer which has zero shear velocity.

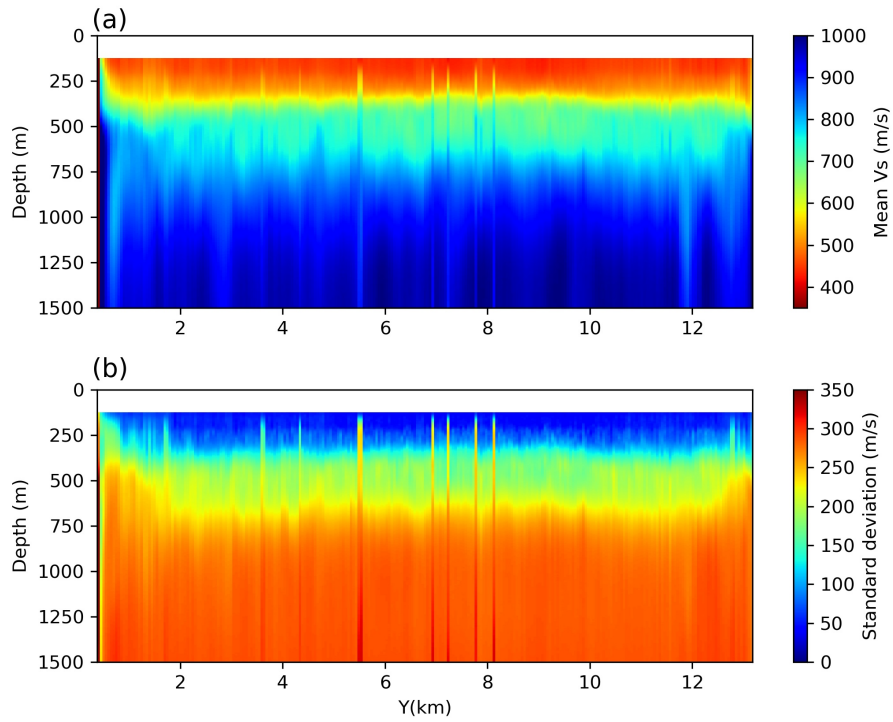


**Figure 22.** (a) Mean and (b) standard deviation from independent 1D Monte Carlo inversions using both the fundamental mode and the first overtone Rayleigh-type Scholte wave phase velocities, with noise levels fixed to be those uncertainties estimated from Eikonal tomography. The white top layer represents the water layer which has zero shear velocity.

870 it has smaller uncertainties ( $\sim 180$  m/s). However, compared to the results from 2D or  
 871 3D inversion, at greater depths (700 - 1000 m) the detailed structure that appeared in  
 872 the 2D and 3D results cannot be observed and the uncertainty is also higher ( $\sim 300$  m/s),  
 873 therefore we still lose some resolution.

874 To conclude, for 1D inversions it is possible that hierarchical Bayesian inversion can  
 875 overfit the data and produce biased results. However, the noise is generally not easy to  
 876 estimate and an improper noise level might also cause model resolution to be lost. By  
 877 including more data (e.g. higher modes dispersion data), this issue can be partly com-  
 878 pensated. Alternatively, we have shown that this issue can also be resolved by includ-  
 879 ing lateral spatial correlations in the inversion using 2D and 3D parameterization.

## 880 6 Discussion

881 We observed two modes in the cross correlations of ambient noise data and used  
 882 a dispersion compensation method to separate those modes. However we have shown that  
 883 even after mode separation there is still some higher mode energy left in the fundamen-  
 884 tal mode estimate at low frequencies, which limits the frequency range used for tomog-  
 885 raphy. Further research needs to be done in order to find methods to use the full frequency  
 886 range of the data and thus to obtain more information from ambient noise cross corre-  
 887 lations. What is more, there is a concern that the higher mode causes errors in the cor-  
 888 relation at the fundamental mode (and vice versa) due to cross-talk in the correlation  
 889 performed in our initial seismic interferometry (Halliday & Curtis, 2008). Unfortunately  
 890 there is little we can do about this as mode separation in the original ambient noise re-  
 891 mains a largely unsolved problem.

892 Our method of dispersion analysis needs an estimate of the phase velocity disper-  
 893 sion to resolve the  $2\pi$  ambiguity in signal phase. This estimate can be obtained using  
 894  $f-c$  analysis in our case, however it is not always possible to obtain an estimate of the  
 895 phase velocity dispersion (e.g. if only a sparse array is available). In such cases some other  
 896 mode separation methods based on single station measurements might be used (Trampert  
 897 & Woodhouse, 1995; van Heijst & Woodhouse, 1997; Kritski et al., 2006).

898 We used Eikonal tomography to determine phase velocity maps by ignoring the am-  
 899 plitude term in equation (4). This is justified when the phase velocity map is sufficient  
 900 smooth so that the spatial variation of amplitude is small (Lin et al., 2009). However,

901 Mordret, Shapiro, et al. (2013) have shown that this could cause some bias in phase ve-  
902 locity maps, especially at long periods (roughly  $> 1.0$  s). According to their study the  
903 bias introduced by ignoring the amplitude term is, on average, about 1 m/s which is far  
904 smaller than our uncertainties. Our results therefore remain valid.

905 In this study, we only used the fundamental mode data when we compared the three  
906 different methods to estimate a 3D shear-velocity model. However, we have also shown  
907 that by including the first overtone dispersion data in 1D inversions, the subsurface struc-  
908 ture can be better constrained, as has been observed previously (Gabriels et al., 1987;  
909 Xia et al., 2000, 2003). Therefore, future work will be to include those first overtone dis-  
910 persion data in the 3D inversion to better constrain the subsurface structure and to fur-  
911 ther improve the resolution of greater depths.

912 We observed a low velocity anomaly at the center of the field both on the funda-  
913 mental mode phase velocity maps at short periods ( $< 1.6$  s) and on the shear velocity  
914 model at shallow depths ( $< 250$  m), which is correlated with a high density region of pock-  
915 mark distribution, suggesting that it might be caused by near surface fluids. Therefore,  
916 such near surface low velocity anomalies might be used as indicators of fluid leakage from  
917 the subsurface reservoirs. This suggests that ambient noise tomography might be used  
918 to monitor subsurface fluid storage reservoirs, for example in CO<sub>2</sub> capture and storage  
919 scenarios.

920 Note that in this study we did not take into account any strong anisotropy which  
921 might exist in the shallow subsurface (Barkved & Kristiansen, 2005; Barkved et al., 2005;  
922 Hatchell et al., 2009). This may introduce some bias in our final results and may explain  
923 the complicated phase velocity structures that we observed at long periods ( $> 1.3$  s) and  
924 the complicated shear velocity structures at depth ( $> 250$  m). However, our results should  
925 at least remain qualitatively valid, and in future it is possible to include anisotropy in  
926 3D Monte Carlo inversions to further improve the results.

927 The MCMC methods are generally very computationally expensive. We now com-  
928 pare the computational cost for the three methods used in this study. For one chain, the  
929 1D depth inversions along the 2D section takes  $\sim 186.1$  cpu hours while the 2D inversion  
930 needs  $\sim 206.8$  cpu hours; 3D inversion costs  $\sim 4824.3$  cpu hours for one chain (but of course  
931 this produces a complete 3D velocity model across the entire area). Thus the 1D and  
932 2D inversions require almost the same cpu hours which makes sense since they are es-

933 essentially the same apart from the different parameterization. Note that the 1D inver-  
 934 sion and the 2D inversion are performed only along one vertical section. If we assume  
 935 that we conduct the 1D inversion and the 2D inversion along all vertical sections in the  
 936 3D grid, (i.e. across all 100 cross-sections included in the grid used in Eikonal tomog-  
 937 raphy), the cpu hours they consumed would be  $\sim 18,610$  cpu hours and 20,680 cpu hours  
 938 respectively – significantly more than for the 3D inversion. However, the computational  
 939 cost in each case strongly depends on the methods used to assess convergence, which in  
 940 turn depend on subjective choices. This therefore introduces some subjectivity to the  
 941 comparison. However, in our experience it is at least true that the cost of the 3D inver-  
 942 sion is comparable to that of the 1D or 2D inversions, which has also been shown by Zhang  
 943 et al. (2018). To provide an overall idea of the computational cost needed for 3D inver-  
 944 sion, the 3D inversion herein takes approximately 22 days with each chain running on  
 945 9 CPU cores, so for all 24 chains it requires 216 CPU cores.

946 Note that in the 3D inversion we used an approximation forward modelling method  
 947 which involves a 1D modal approximation and a 2D fast marching method. Although  
 948 the method improves the accuracy of the results, the use of 1D forward modelling and  
 949 3D parametrization could fail to accurately capture the underlying properties and struc-  
 950 tures. For example, D. Yang and Oldenburg (2012) showed that 1D inversion can cause  
 951 artefacts in the final results compared to a 3D inversion when using airborne time-domain  
 952 electromagnetic data. Thus, in the future we hope to use a more accurate forward mod-  
 953 elling method.

## 954 **7 Conclusion**

955 We cross correlated about 6.5 hours of ambient noise data from the Grane field,  
 956 North sea and observed two modes in the constructed seabed Scholte waves. The fun-  
 957 damental mode dominates the signal in the cross correlations of vertical component dis-  
 958 placement data while the first overtone dominates in the cross correlations of hydrophone  
 959 components. We used a dispersion compensation method to separate the fundamental  
 960 mode and the first overtone. For each mode, we determined phase velocity maps at dif-  
 961 ferent periods using the Eikonal tomography method. The fundamental mode phase ve-  
 962 locity maps show a low velocity anomaly at the center of the area at short periods ( $<$   
 963 1.6 s), which might be caused by near surface fluids. At longer periods both modes show

964 complicated phase velocity structures, suggesting that the Grane field might have a com-  
965 plicated geological subsurface.

966 We then applied three different methods, 1D, 2D and 3D Monte Carlo inversions,  
967 to obtain shear wave velocity models of the subsurface using dispersion data of the fun-  
968 damental mode as data and compared the results. The 1D results show complicated struc-  
969 tures at deeper depths ( $> 250$  m) which are probably caused by the independence of in-  
970 dividual 1D inversions since the discontinuous structures do not appear in the 2D and  
971 3D results. By including the lateral spatial correlations in the 2D and 3D inversions, we  
972 may estimate a more realistic model. The 2D inversion and the 3D inversion show lower  
973 uncertainties at greater depths (500 - 750 m), which suggests that the 2D and 3D inver-  
974 sion allow greater confidence at larger depths than the 1D inversion. The 3D inversion  
975 results better match a model obtained from reflection tomography than do the results  
976 from 2D or 1D inversions. This is probably due to the fact that the 3D inversion uses  
977 the measured source-to-receiver travel times directly, and therefore naturally avoids pos-  
978 sible errors introduced in the initial (Eikonal) phase velocity tomography step required  
979 by the other methods. Though the 3D velocity model is determined using only the fun-  
980 damental mode dispersion data, it shows some similar features to those which appear  
981 in the phase velocity maps of the first overtone. This provides a validation of our 3D re-  
982 sults and may suggest that the complex phase velocity maps at longer periods could pro-  
983 vide some useful information of the subsurface structure. Overall, the 3D MCMC method  
984 provides an accurate way to study the subsurface structure using surface wave disper-  
985 sion data and it is also roughly as computationally efficient as similar 1D and 2D two-  
986 step MCMC inversions.

## 987 **Acknowledgments**

988 The authors would like to thank the Grane license partners Equinor ASA, Petoro AS,  
989 ExxonMobil E&P Norway AS, and ConocoPhillips Skandinavia AS for allowing us to  
990 publish this work. The views and opinions expressed in this paper are those of the au-  
991 thors and are not necessarily shared by the license partners. The authors thank the Ed-  
992 inburgh Interferometry Project sponsors (Schlumberger, Equinor and Total) for support-  
993 ing this research. This work used the Cirrus UK National Tier-2 HPC Service at EPCC  
994 (<http://www.cirrus.ac.uk>). The dispersion curve data used in this study are available  
995 at Edinburgh DataShare (<https://datashare.is.ed.ac.uk/handle/10283/3398>). The raw

996 data may be requested from the Grane license partners Equinor ASA, Petoro As, Exxon-  
 997 Mobil E&P Norway AS, and ConocoPhillips Skandinavia AS.

## 998 **References**

- 999 Aki, K., & Richards, P. G. (1980). *Quantitative seismology*.
- 1000 Alleyne, D., Pialucha, T., & Cawley, P. (1993). A signal regeneration technique for  
 1001 long-range propagation of dispersive lamb waves. *Ultrasonics*, *31*(3), 201–204.
- 1002 Allmark, C., Curtis, A., Galetti, E., & de Ridder, S. (2018). Seismic attenuation  
 1003 from ambient noise across the North Sea Ekofisk permanent array. *Journal of*  
 1004 *Geophysical Research: Solid Earth*.
- 1005 Barkved, O. I., & Kristiansen, T. (2005). Seismic time-lapse effects and stress  
 1006 changes: Examples from a compacting reservoir. *The Leading Edge*, *24*(12),  
 1007 1244–1248.
- 1008 Barkved, O. I., Kristiansen, T., & Fjær, E. (2005). The 4D seismic response of a  
 1009 compacting reservoir examples from the Valhall field, Norway. In *Seg technical*  
 1010 *program expanded abstracts 2005* (pp. 2508–2511). Society of Exploration Geo-  
 1011 physicists.
- 1012 Behr, Y., Townend, J., Bannister, S., & Savage, M. (2010). Shear velocity struc-  
 1013 ture of the Northland Peninsula, New Zealand, inferred from ambient noise  
 1014 correlations. *Journal of Geophysical Research: Solid Earth*, *115*(B5).
- 1015 Belhadj, J., Romary, T., Gesret, A., Noble, M., & Figliuzzi, B. (2018). New parame-  
 1016 terizations for bayesian seismic tomography. *Inverse Problems*, *34*(6), 065007.
- 1017 Bensen, G., Ritzwoller, M., & Yang, Y. (2009). A 3-D shear velocity model of the  
 1018 crust and uppermost mantle beneath the United States from ambient seismic  
 1019 noise. *Geophysical Journal International*, *177*(3), 1177–1196.
- 1020 Biondi, B. (1992). Solving the frequency-dependent Eikonal equation. In *Seg tech-*  
 1021 *nical program expanded abstracts 1992* (pp. 1315–1319). Society of Exploration  
 1022 Geophysicists.
- 1023 Bodin, T., & Sambridge, M. (2009). Seismic tomography with the reversible jump  
 1024 algorithm. *Geophysical Journal International*, *178*(3), 1411–1436.
- 1025 Bodin, T., Sambridge, M., Tkalčić, H., Arroucau, P., Gallagher, K., & Rawlinson,  
 1026 N. (2012). Transdimensional inversion of receiver functions and surface wave  
 1027 dispersion. *Journal of Geophysical Research: Solid Earth*, *117*(B2).

- 1028 Brocher, T. M. (2005). Empirical relations between elastic wavespeeds and density  
 1029 in the earth's crust. *Bulletin of the seismological Society of America*, *95*(6),  
 1030 2081–2092.
- 1031 Bullock, A., Bekhtin, Y., Ortin, M., Mathewson, J., Henneberg, K., & Sæbø, A.  
 1032 (2015). Improved imaging with PP-PS simultaneous joint tomography over the  
 1033 Grane field. In *Seg technical program expanded abstracts 2015* (pp. 2094–2097).  
 1034 Society of Exploration Geophysicists.
- 1035 Burdick, S., & Lekić, V. (2017). Velocity variations and uncertainty from transdi-  
 1036 mensional p-wave tomography of North America. *Geophysical Journal Interna-*  
 1037 *tional*, *209*(2), 1337–1351.
- 1038 Calderhead, B., & Girolami, M. (2009). Estimating Bayes factors via thermody-  
 1039 namic integration and population MCMC. *Computational Statistics & Data*  
 1040 *Analysis*, *53*(12), 4028–4045.
- 1041 Campillo, M., & Paul, A. (2003). Long-range correlations in the diffuse seismic coda.  
 1042 *Science*, *299*(5606), 547–549.
- 1043 Castagna, J. P., Batzle, M. L., & Eastwood, R. L. (1985). Relationships between  
 1044 compressional-wave and shear-wave velocities in clastic silicate rocks. *Geo-*  
 1045 *physics*, *50*(4), 571–581.
- 1046 Chen, X. (1993). A systematic and efficient method of computing normal modes for  
 1047 multilayered half-space. *Geophysical Journal International*, *115*(2), 391–409.
- 1048 Chmiel, M., Mordret, A., Boué, P., Brenguier, F., Lecocq, T., Courbis, R., . . .  
 1049 Van der Veen, W. (2019). Ambient noise multimode rayleigh and love wave  
 1050 tomography to determine the shear velocity structure above the groningen gas  
 1051 field. *Geophysical Journal International*, *218*(3), 1781–1795.
- 1052 Cole, S. P. (1995). *Passive seismic and drill-bit experiments using 2-D arrays*  
 1053 (No. 86). Stanford University.
- 1054 Crampin, S., & Båth, M. (1965). Higher modes of seismic surface waves: mode sepa-  
 1055 ration. *Geophysical Journal International*, *10*(1), 81–92.
- 1056 Curtis, A., Gerstoft, P., Sato, H., Snieder, R., & Wapenaar, K. (2006). Seismic inter-  
 1057 ferometry – turning noise into signal. *The Leading Edge*, *25*(9), 1082–1092.
- 1058 Curtis, A., & Halliday, D. (2010). Directional balancing for seismic and general  
 1059 wavefield interferometry. *Geophysics*, *75*(1), SA1–SA14.
- 1060 Curtis, A., Trampert, J., Snieder, R., & Dost, B. (1998). Eurasian fundamental

- 1061 mode surface wave phase velocities and their relationship with tectonic struc-  
1062 tures. *Journal of Geophysical Research: Solid Earth*, *103*(B11), 26919–26947.
- 1063 de Ridder, S., & Biondi, B. (2013). Daily reservoir-scale subsurface monitoring using  
1064 ambient seismic noise. *Geophysical Research Letters*, *40*(12), 2969–2974.
- 1065 de Ridder, S., Biondi, B., & Clapp, R. (2014). Time-lapse seismic noise correlation  
1066 tomography at Valhall. *Geophysical Research Letters*, *41*(17), 6116–6122.
- 1067 de Ridder, S., Biondi, B., & Nichols, D. (2015). Elliptical-anisotropic Eikonal phase  
1068 velocity tomography. *Geophysical Research Letters*, *42*(3), 758–764.
- 1069 de Ridder, S., & Dellinger, J. (2011). Ambient seismic noise Eikonal tomography for  
1070 near-surface imaging at Valhall. *The Leading Edge*, *30*(5), 506–512.
- 1071 Dettmer, J., & Dosso, S. E. (2012). Trans-dimensional matched-field geoacoustic  
1072 tic inversion with hierarchical error models and interacting Markov chains. *The*  
1073 *Journal of the Acoustical Society of America*, *132*(4), 2239–2250.
- 1074 Dettmer, J., Hawkins, R., Cummins, P. R., Hossen, J., Sambridge, M., Hino, R., &  
1075 Inazu, D. (2016). Tsunami source uncertainty estimation: The 2011 japan  
1076 tsunami. *Journal of Geophysical Research: Solid Earth*, *121*(6), 4483–4505.
- 1077 Dosso, S. E., Dettmer, J., Steininger, G., & Holland, C. W. (2014). Efficient trans-  
1078 dimensional Bayesian inversion for geoacoustic profile estimation. *Inverse*  
1079 *Problems*, *30*(11), 114018.
- 1080 Dosso, S. E., Holland, C. W., & Sambridge, M. (2012). Parallel tempering for  
1081 strongly nonlinear geoacoustic inversion. *The Journal of the Acoustical Society*  
1082 *of America*, *132*(5), 3030–3040.
- 1083 Dziewonski, A., Bloch, S., & Landisman, M. (1969). A technique for the analysis  
1084 of transient seismic signals. *Bulletin of the seismological Society of America*,  
1085 *59*(1), 427–444.
- 1086 Earl, D. J., & Deem, M. W. (2005). Parallel tempering: Theory, applications, and  
1087 new perspectives. *Physical Chemistry Chemical Physics*, *7*(23), 3910–3916.
- 1088 Ekström, G. (2011). A global model of Love and Rayleigh surface wave dispersion  
1089 and anisotropy, 25-250 s. *Geophysical Journal International*, *187*(3), 1668–  
1090 1686.
- 1091 Fang, H., Yao, H., Zhang, H., Huang, Y.-C., & van der Hilst, R. D. (2015). Direct  
1092 inversion of surface wave dispersion for three-dimensional shallow crustal struc-  
1093 ture based on ray tracing: methodology and application. *Geophysical Journal*

- 1094 *International*, 201(3), 1251–1263.
- 1095 Ferreira, A., Woodhouse, J., Visser, K., & Trampert, J. (2010). On the robustness  
1096 of global radially anisotropic surface wave tomography. *Journal of Geophysical*  
1097 *Research: Solid Earth*, 115(B4).
- 1098 Fink, M. (1992). Time reversal of ultrasonic fields. i. basic principles. *IEEE transac-*  
1099 *tions on ultrasonics, ferroelectrics, and frequency control*, 39(5), 555–566.
- 1100 Gabriels, P., Snieder, R., & Nolet, G. (1987). In situ measurements of shear-wave ve-  
1101 locity in sediments with higher-mode Rayleigh waves. *Geophysical prospecting*,  
1102 35(2), 187–196.
- 1103 Galetti, E., & Curtis, A. (2018). Transdimensional electrical resistivity tomography.  
1104 *Journal of Geophysical Research: Solid Earth*, 123(8), 6347–6377.
- 1105 Galetti, E., Curtis, A., Baptie, B., Jenkins, D., & Nicolson, H. (2017). Transdimen-  
1106 sional Love-wave tomography of the British Isles and shear-velocity structure  
1107 of the east Irish Sea Basin from ambient-noise interferometry. *Geophysical*  
1108 *Journal International*, 208(1), 36–58.
- 1109 Galetti, E., Curtis, A., Meles, G. A., & Baptie, B. (2015). Uncertainty loops in  
1110 travel-time tomography from nonlinear wave physics. *Physical review letters*,  
1111 114(14), 148501.
- 1112 Geyer, C. J. (1994). Estimating normalizing constants and reweighting mixtures.  
1113 *Technical Report*.
- 1114 Green, P. J. (1995). Reversible jump Markov chain Monte Carlo computation and  
1115 Bayesian model determination. *Biometrika*, 711–732.
- 1116 Green, P. J., & Hastie, D. I. (2009). Reversible jump MCMC. *Genetics*, 155(3),  
1117 1391–1403.
- 1118 Halliday, D., & Curtis, A. (2008). Seismic interferometry, surface waves and source  
1119 distribution. *Geophysical Journal International*, 175(3), 1067–1087.
- 1120 Hastings, W. K. (1970). Monte Carlo sampling methods using Markov chains and  
1121 their applications. *Biometrika*, 57(1), 97–109.
- 1122 Hatchell, P., Wills, P., & Didraga, C. (2009). Production induced effects on near-  
1123 surface wave velocities at Valhall. In *71st eage conference and exhibition incor-*  
1124 *porating spe europec 2009*.
- 1125 Hawkins, R., Bodin, T., Sambridge, M., Choblet, G., & Husson, L. (2019). Trans-  
1126 dimensional surface reconstruction with different classes of parameterization.

- 1127           *Geochemistry, Geophysics, Geosystems*, 20(1), 505–529.
- 1128   Hawkins, R., & Sambridge, M. (2015). Geophysical imaging using trans-dimensional  
1129           trees. *Geophysical Journal International*, 203(2), 972–1000.
- 1130   Herrin, E., & Goforth, T. (1977). Phase-matched filters: application to the study of  
1131           Rayleigh waves. *Bulletin of the Seismological Society of America*, 67(5), 1259–  
1132           1275.
- 1133   Herrmann, R. B. (2013). Computer programs in seismology: An evolving tool for in-  
1134           struction and research. *Seismological Research Letters*, 84(6), 1081–1088.
- 1135   Ing, R. K., & Fink, M. (1998). Time-reversed lamb waves. *IEEE transactions on ul-*  
1136           *trasonics, ferroelectrics, and frequency control*, 45(4), 1032–1043.
- 1137   Jan van Heijst, H., & Woodhouse, J. (1999). Global high-resolution phase velocity  
1138           distributions of overtone and fundamental-mode surface waves determined by  
1139           mode branch stripping. *Geophysical Journal International*, 137(3), 601–620.
- 1140   Khan, A., Zunino, A., & Deschamps, F. (2013). Upper mantle compositional vari-  
1141           ations and discontinuity topography imaged beneath Australia from Bayesian  
1142           inversion of surface-wave phase velocities and thermochemical modeling. *Jour-*  
1143           *nal of Geophysical Research: Solid Earth*, 118(10), 5285–5306.
- 1144   Kritski, A., Vincent, A., Yuen, D., & Carlsen, T. (2006). Adaptive wavelets for ana-  
1145           lyzing dispersive seismic waves. *Geophysics*, 72(1), V1–V11.
- 1146   Kuttig, H., Niethammer, M., Hurlebaus, S., & Jacobs, L. J. (2006). Model-based  
1147           analysis of dispersion curves using chirplets. *The Journal of the Acoustical So-*  
1148           *ciety of America*, 119(4), 2122–2130.
- 1149   Kvenvolden, K. A. (1989). Seabed pockmarks and seepages: Impact on geology, biol-  
1150           ogy and the marine environment. *Science*, 244(4904), 590–592.
- 1151   Levshin, A., Ratnikova, L., & Berger, J. (1992). Peculiarities of surface-wave propa-  
1152           gation across central Eurasia. *Bulletin of the Seismological Society of America*,  
1153           82(6), 2464–2493.
- 1154   Levshin, A., & Ritzwoller, M. (2001). Automated detection, extraction, and mea-  
1155           surement of regional surface waves. In *Monitoring the comprehensive nuclear-*  
1156           *test-ban treaty: Surface waves* (pp. 1531–1545). Springer.
- 1157   Levshin, A. L., Pisarenko, V., & Pogrebinsky, G. (1972). On a frequency-time analy-  
1158           sis of oscillations. In *Annales de geophysique* (Vol. 28, pp. 211–218).
- 1159   Lin, F.-C., Moschetti, M. P., & Ritzwoller, M. H. (2008). Surface wave tomogra-

- 1160 phy of the western United States from ambient seismic noise: Rayleigh and  
1161 Love wave phase velocity maps. *Geophysical Journal International*, *173*(1),  
1162 281–298.
- 1163 Lin, F.-C., Ritzwoller, M. H., & Snieder, R. (2009). Eikonal tomography: surface  
1164 wave tomography by phase front tracking across a regional broad-band seismic  
1165 array. *Geophysical Journal International*, *177*(3), 1091–1110.
- 1166 Lin, F.-C., Ritzwoller, M. H., Townend, J., Bannister, S., & Savage, M. K. (2007).  
1167 Ambient noise Rayleigh wave tomography of New Zealand. *Geophysical Jour-*  
1168 *nal International*, *170*(2), 649–666.
- 1169 Malinverno, A. (2002). Parsimonious Bayesian Markov chain Monte Carlo inversion  
1170 in a nonlinear geophysical problem. *Geophysical Journal International*, *151*(3),  
1171 675–688.
- 1172 Malinverno, A., & Briggs, V. A. (2004). Expanded uncertainty quantification in  
1173 inverse problems: Hierarchical Bayes and empirical Bayes. *Geophysics*, *69*(4),  
1174 1005–1016.
- 1175 Malinverno, A., Leaney, S., et al. (2000). A Monte Carlo method to quantify uncer-  
1176 tainty in the inversion of zero-offset VSP data. In *2000 seg annual meeting*.
- 1177 Meier, U., Curtis, A., & Trampert, J. (2007a). A global crustal model constrained  
1178 by nonlinearised inversion of fundamental mode surface waves. *Geophysical Re-*  
1179 *search Letters*, *34*, L16304.
- 1180 Meier, U., Curtis, A., & Trampert, J. (2007b). Global crustal thickness from neu-  
1181 ral network inversion of surface wave data. *Geophysical Journal International*,  
1182 *169*(2), 706–722.
- 1183 Metropolis, N., & Ulam, S. (1949). The Monte Carlo method. *Journal of the Ameri-*  
1184 *can statistical association*, *44*(247), 335–341.
- 1185 Mordret, A., Landès, M., Shapiro, N., Singh, S., & Roux, P. (2014). Ambient noise  
1186 surface wave tomography to determine the shallow shear velocity structure at  
1187 Valhall: depth inversion with a neighbourhood algorithm. *Geophysical Journal*  
1188 *International*, *198*(3), 1514–1525.
- 1189 Mordret, A., Landès, M., Shapiro, N., Singh, S., Roux, P., & Barkved, O. (2013).  
1190 Near-surface study at the Valhall oil field from ambient noise surface wave  
1191 tomography. *Geophysical Journal International*, *193*(3), 1627–1643.
- 1192 Mordret, A., Shapiro, N. M., & Singh, S. (2014). Seismic noise-based time-lapse

- 1193 monitoring of the Valhall overburden. *Geophysical Research Letters*, *41*(14),  
 1194 4945–4952.
- 1195 Mordret, A., Shapiro, N. M., Singh, S. S., Roux, P., & Barkved, O. I. (2013).  
 1196 Helmholtz tomography of ambient noise surface wave data to estimate Scholte  
 1197 wave phase velocity at Valhall life of the fieldnoise tomography at Valhall.  
 1198 *Geophysics*, *78*(2), WA99–WA109.
- 1199 Mosegaard, K., & Tarantola, A. (1995). Monte Carlo sampling of solutions to  
 1200 inverse problems. *Journal of Geophysical Research: Solid Earth*, *100*(B7),  
 1201 12431–12447.
- 1202 Nakanishi, I., & Anderson, D. L. (1983). Measurement of mantle wave velocities  
 1203 and inversion for lateral heterogeneity and anisotropy: 1. analysis of great cir-  
 1204 cle phase velocities. *Journal of Geophysical Research: Solid Earth*, *88*(B12),  
 1205 10267–10283.
- 1206 Nicolson, H., Curtis, A., & Baptie, B. (2014). Rayleigh wave tomography of the  
 1207 British Isles from ambient seismic noise. *Geophysical Journal International*,  
 1208 *198*(2), 637–655.
- 1209 Nicolson, H., Curtis, A., Baptie, B., & Galetti, E. (2012). Seismic interferometry  
 1210 and ambient noise tomography in the British Isles. *Proceedings of the Geolo-  
 1211 gists' Association*, *123*(1), 74–86.
- 1212 Park, C. B., Miller, R. D., & Xia, J. (1999). Multichannel analysis of surface waves.  
 1213 *Geophysics*, *64*(3), 800–808.
- 1214 Park, C. B., Miller, R. D., Xia, J., Hunter, J. A., & Harris, J. B. (1999). Higher  
 1215 mode observation by the MASW method. In *Seg technical program expanded  
 1216 abstracts 1999* (pp. 524–527). Society of Exploration Geophysicists.
- 1217 Piana Agostinetti, N., Giacomuzzi, G., & Malinverno, A. (2015). Local three-  
 1218 dimensional earthquake tomography by trans-dimensional Monte Carlo sam-  
 1219 pling. *Geophysical Journal International*, *201*(3), 1598–1617.
- 1220 Pragt, J., Herberg, W., Meister, M., Clemmensen, C. C., Grindhaug, G., Hanken,  
 1221 K. J., et al. (2012). Reaming on demand-selective activation of an integrated  
 1222 under reamer at the Grane field in the North Sea. In *Spe deepwater drilling  
 1223 and completions conference*.
- 1224 Rawlinson, N., Fichtner, A., Sambridge, M., & Young, M. K. (2014). Seismic tomog-  
 1225 raphy and the assessment of uncertainty. In *Advances in geophysics* (Vol. 55,

- 1226 pp. 1–76). Elsevier.
- 1227 Rawlinson, N., & Sambridge, M. (2004). Multiple reflection and transmission  
1228 phases in complex layered media using a multistage fast marching method.  
1229 *Geophysics*, *69*(5), 1338–1350.
- 1230 Ray, A., Kaplan, S., Washbourne, J., & Albertin, U. (2017). Low frequency full  
1231 waveform seismic inversion within a tree based Bayesian framework. *Geophysi-  
1232 cal Journal International*, *212*(1), 522–542.
- 1233 Reiter, D. T., & Rodi, W. L. (2008). *A new regional 3-D velocity model for Asia  
1234 from the joint inversion of p-wave travel times and surface-wave dispersion  
1235 data* (Tech. Rep.). WESTON GEOPHYSICAL LEXINGTON MA.
- 1236 Ritzwoller, M. H., & Levshin, A. L. (1998). Eurasian surface wave tomography:  
1237 Group velocities. *Journal of Geophysical Research: Solid Earth*, *103*(B3),  
1238 4839–4878.
- 1239 Ritzwoller, M. H., Shapiro, N. M., Barmin, M. P., & Levshin, A. L. (2002). Global  
1240 surface wave diffraction tomography. *Journal of Geophysical Research: Solid  
1241 Earth*, *107*(B12).
- 1242 Rost, S., & Thomas, C. (2002). Array seismology: Methods and applications. *Re-  
1243 views of geophysics*, *40*(3), 2–1.
- 1244 Russell, D. R., Herrmann, R. B., & Hwang, H.-J. (1988). Application of frequency  
1245 variable filters to surface-wave amplitude analysis. *Bulletin of the Seismological  
1246 Society of America*, *78*(1), 339–354.
- 1247 Saito, M. (1988). DISPER80: A subroutine package for the calculation of seismic  
1248 normal-mode solutions. *Seismological algorithms*, 293–319.
- 1249 Sambridge, M. (2013). A parallel tempering algorithm for probabilistic sampling and  
1250 multimodal optimization. *Geophysical Journal International*, ggt342.
- 1251 Savage, M. K., Lin, F.-C., & Townend, J. (2013). Ambient noise cross-correlation  
1252 observations of fundamental and higher-mode rayleigh wave propagation gov-  
1253 erned by basement resonance. *Geophysical Research Letters*, *40*(14), 3556–  
1254 3561.
- 1255 Saygin, E., Cummins, P., Cipta, A., Hawkins, R., Pandhu, R., Murjaya, J., . . . Ken-  
1256 nett, B. (2015). Imaging architecture of the Jakarta Basin, Indonesia with  
1257 transdimensional inversion of seismic noise. *Geophysical Journal International*,  
1258 *204*(2), 918–931.

- 1259 Sengupta, B., Friston, K. J., & Penny, W. D. (2015). Gradient-free MCMC methods  
1260 for dynamic causal modelling. *NeuroImage*, *112*, 375–381.
- 1261 Shapiro, N., & Ritzwoller, M. (2002). Monte-Carlo inversion for a global shear-  
1262 velocity model of the crust and upper mantle. *Geophysical Journal Interna-*  
1263 *tional*, *151*(1), 88–105.
- 1264 Shapiro, N. M., & Campillo, M. (2004). Emergence of broadband Rayleigh waves  
1265 from correlations of the ambient seismic noise. *Geophysical Research Letters*,  
1266 *31*(7).
- 1267 Shapiro, N. M., Campillo, M., Stehly, L., & Ritzwoller, M. H. (2005). High-  
1268 resolution surface-wave tomography from ambient seismic noise. *Science*,  
1269 *307*(5715), 1615–1618.
- 1270 Shearer, P. (1999). *Introduction to seismology*. Cambridge University Press.
- 1271 Shen, W., Ritzwoller, M. H., & Schulte-Pelkum, V. (2013). A 3-D model of the crust  
1272 and uppermost mantle beneath the central and western US by joint inver-  
1273 sion of receiver functions and surface wave dispersion. *Journal of Geophysical*  
1274 *Research: Solid Earth*, *118*(1), 262–276.
- 1275 Shen, W., Ritzwoller, M. H., Schulte-Pelkum, V., & Lin, F.-C. (2012). Joint inver-  
1276 sion of surface wave dispersion and receiver functions: a Bayesian Monte-Carlo  
1277 approach. *Geophysical Journal International*, *192*(2), 807–836.
- 1278 Simons, F. J., Van Der Hilst, R. D., Montagner, J.-P., & Zielhuis, A. (2002). Mul-  
1279 timode Rayleigh wave inversion for heterogeneity and azimuthal anisotropy  
1280 of the Australian upper mantle. *Geophysical Journal International*, *151*(3),  
1281 738–754.
- 1282 Sivia, D. (1996). *Data analysis: A Bayesian tutorial* (oxford science publications).
- 1283 Snoke, J. A., & Sambridge, M. (2002). Constraints on the S wave velocity struc-  
1284 ture in a continental shield from surface wave data: Comparing linearized least  
1285 squares inversion and the direct search neighbourhood algorithm. *Journal of*  
1286 *Geophysical Research: Solid Earth*, *107*(B5).
- 1287 Stevens, J. L., Adams, D. A., & Baker, G. E. (2001). *Improved surface wave detec-*  
1288 *tion and measurement using phase-matched filtering with a global one-degree*  
1289 *dispersion model* (Tech. Rep.). SCIENCE APPLICATIONS INTERNA-  
1290 TIONAL CORP SAN DIEGO CA.
- 1291 Thompson, M., Andersen, M., Elde, R., Roy, S., & Skogland, S. (2015). The startup

- 1292 of permanent reservoir monitoring for snorre and grane. In *77th eage confer-*  
 1293 *ence and exhibition 2015*.
- 1294 Tomar, G., Stutzmann, E., Mordret, A., Montagner, J.-P., Singh, S. C., & Shapiro,  
 1295 N. M. (2018). Joint inversion of the first overtone and fundamental mode for  
 1296 deep imaging at the valhall oil field using ambient noise. *Geophysical Journal*  
 1297 *International*, *214*(1), 122–132.
- 1298 Trampert, J., & Woodhouse, J. H. (1995). Global phase velocity maps of Love  
 1299 and Rayleigh waves between 40 and 150 seconds. *Geophysical Journal Interna-*  
 1300 *tional*, *122*(2), 675–690.
- 1301 van Heijst, H. J., & Woodhouse, J. (1997). Measuring surface-wave overtone phase  
 1302 velocities using a mode-branch stripping technique. *Geophysical Journal Inter-*  
 1303 *national*, *131*(2), 209–230.
- 1304 van Manen, D.-J., Curtis, A., & Robertsson, J. O. (2006). Interferometric modeling  
 1305 of wave propagation in inhomogeneous elastic media using time reversal and  
 1306 reciprocity. *Geophysics*, *71*(4), SI47–SI60.
- 1307 van Manen, D.-J., Robertsson, J. O., & Curtis, A. (2005). Modeling of wave propa-  
 1308 gation in inhomogeneous media. *Physical Review Letters*, *94*(16), 164301.
- 1309 Wapenaar, K. (2004). Retrieving the elastodynamic green’s function of an arbitrary  
 1310 inhomogeneous medium by cross correlation. *Physical review letters*, *93*(25),  
 1311 254301.
- 1312 Wapenaar, K., & Fokkema, J. (2006). Greens function representations for seismic in-  
 1313 terferometry. *Geophysics*, *71*(4), SI33–SI46.
- 1314 Weaver, R. L., Hadziioannou, C., Larose, E., & Campillo, M. (2011). On the pre-  
 1315 cision of noise correlation interferometry. *Geophysical Journal International*,  
 1316 *185*(3), 1384–1392.
- 1317 Webb, S. C. (1998). Broadband seismology and noise under the ocean. *Reviews of*  
 1318 *Geophysics*, *36*(1), 105–142.
- 1319 Wielandt, E. (1993). Propagation and structural interpretation of non-plane waves.  
 1320 *Geophysical Journal International*, *113*(1), 45–53.
- 1321 Wilcox, P. D. (2003). A rapid signal processing technique to remove the effect of  
 1322 dispersion from guided wave signals. *IEEE transactions on ultrasonics, ferro-*  
 1323 *electrics, and frequency control*, *50*(4), 419–427.
- 1324 Wu, B., & Chen, X. (2016). Stable, accurate and efficient computation of normal

- 1325 modes for horizontal stratified models. *Geophysical Journal International*,  
1326 *206*(2), 1281–1300.
- 1327 Xia, J., Miller, R. D., & Park, C. B. (2000). Advantages of calculating shear-wave  
1328 velocity from surface waves with higher modes. In *Seg technical program ex-*  
1329 *expanded abstracts 2000* (pp. 1295–1298). Society of Exploration Geophysicists.
- 1330 Xia, J., Miller, R. D., Park, C. B., & Tian, G. (2003). Inversion of high frequency  
1331 surface waves with fundamental and higher modes. *Journal of Applied Geo-*  
1332 *physics*, *52*(1), 45–57.
- 1333 Xu, K., Ta, D., Moilanen, P., & Wang, W. (2012). Mode separation of lamb waves  
1334 based on dispersion compensation method. *The Journal of the Acoustical Soci-*  
1335 *ety of America*, *131*(4), 2714–2722.
- 1336 Yang, D., & Oldenburg, D. W. (2012). Three-dimensional inversion of airborne  
1337 time-domain electromagnetic data with applications to a porphyry deposit.  
1338 *Geophysics*, *77*(2), B23–B34.
- 1339 Yang, Y., Ritzwoller, M. H., Levshin, A. L., & Shapiro, N. M. (2007). Ambient noise  
1340 Rayleigh wave tomography across Europe. *Geophysical Journal International*,  
1341 *168*(1), 259–274.
- 1342 Yanovskaya, T., Levshin, A., Its, E., Lander, A., Bukchin, B., Barmin, M., & Rat-  
1343 nikova, L. (2012). *Seismic surface waves in a laterally inhomogeneous Earth*  
1344 (Vol. 9). Springer Science & Business Media.
- 1345 Yao, H., & Van Der Hilst, R. D. (2009). Analysis of ambient noise energy distribu-  
1346 tion and phase velocity bias in ambient noise tomography, with application to  
1347 SE Tibet. *Geophysical Journal International*, *179*(2), 1113–1132.
- 1348 Yao, H., van Der Hilst, R. D., & De Hoop, M. V. (2006). Surface-wave array tomog-  
1349 raphy in SE tibet from ambient seismic noise and two-station analysis-i. phase  
1350 velocity maps. *Geophysical Journal International*, *166*(2), 732–744.
- 1351 Yilmaz, Ö. (2001). *Seismic data analysis* (Vol. 1). Society of exploration geophysi-  
1352 cists.
- 1353 Young, M. K., Rawlinson, N., & Bodin, T. (2013). Transdimensional inversion of  
1354 ambient seismic noise for 3D shear velocity structure of the Tasmanian crust.  
1355 *Geophysics*, *78*(3), WB49–WB62.
- 1356 Zhang, X., Curtis, A., Galetti, E., & de Ridder, S. (2018). 3-D Monte Carlo surface  
1357 wave tomography. *Geophysical Journal International*, *215*(3), 1644–1658.

- 1358 Zhdanov, M. S. (2002). *Geophysical inverse theory and regularization problems*  
1359 (Vol. 36). Elsevier.
- 1360 Zheng, D., Saygin, E., Cummins, P., Ge, Z., Min, Z., Cipta, A., & Yang, R. (2017).  
1361 Transdimensional Bayesian seismic ambient noise tomography across SE Tibet.  
1362 *Journal of Asian Earth Sciences*, *134*, 86–93.
- 1363 Zielhuis, A., & Nolet, G. (1994). Deep seismic expression of an ancient plate bound-  
1364 ary in Europe. *Science*, *265*(5168), 79–81.
- 1365 Zigone, D., Ben-Zion, Y., Campillo, M., & Roux, P. (2015). Seismic tomography of  
1366 the Southern California plate boundary region from noise-based Rayleigh and  
1367 Love waves. *Pure and Applied Geophysics*, *172*(5), 1007–1032.
- 1368 Zulfakriza, Z., Saygin, E., Cummins, P., Widiyantoro, S., Nugraha, A. D., Lühr,  
1369 B.-G., & Bodin, T. (2014). Upper crustal structure of central Java, Indonesia,  
1370 from transdimensional seismic ambient noise tomography. *Geophysical Journal*  
1371 *International*, *197*(1), 630–635.